A&A 656, A154 (2021)
https://doi.org/10.1051/0004-6361/202141428
© ESO 2021

Astronomy & Astrophysics

A 3.5 Mpc long radio relic in the galaxy cluster ClG 0217+70★

D. N. Hoang[1], X. Zhang[2,3], C. Stuardi[4,5], T. W. Shimwell[6,2], A. Bonafede[4,5], M. Brüggen[1], G. Brunetti[5], A. Botteon[2], R. Cassano[5], F. de Gasperin[1,5], G. Di Gennaro[1,2], M. Hoeft[9], H. Intema[2], K. Rajpurohit[4], H. J. A. Röttgering[2], A. Simionescu[3,2,7], and R. J. van Weeren[2,8]

[1] Hamburger Sternwarte, University of Hamburg, Gojenbergsweg 112, 21029 Hamburg, Germany
e-mail: hoang@hs.uni-hamburg.de
[2] Leiden Observatory, Leiden University, PO Box 9513, 2300 RA Leiden, The Netherlands
[3] SRON Netherlands Institute for Space Research, Sorbonnelaan 2, 3584 CA Utrecht, The Netherlands
[4] Dipartimento di Fisica e Astronomia, Universitá di Bologna, via Gobetti 93/2, 40122 Bologna, Italy
[5] INAF – Istituto di Radioastronomia di Bologna, Via Gobetti 101, 40129 Bologna, Italy
[6] Netherlands Institute for Radio Astronomy (ASTRON), PO Box 2, 7990 AA Dwingeloo, The Netherlands
[7] Kavli Institute for the Physics and Mathematics of the Universe (WPI), The University of Tokyo, Kashiwa, Chiba 277-8583, Japan
[8] Harvard-Smithsonian Center for Astrophysics, 60 Garden Street, Cambridge, MA 02138, USA
[9] Thüringer Landessternwarte, Sternwarte 5, 07778 Tautenburg, Germany

Received 30 May 2021 / Accepted 2 October 2021

ABSTRACT

Context. Megaparsec-scale radio sources in the form of halos and relics are often detected in dynamically disturbed galaxy clusters. Although they are associated with merger-induced turbulence and shocks, respectively, their formation is not fully understood.
Aims. We aim to identify the mechanisms responsible for particle acceleration and magnetic field amplification in the halo and relics of the galaxy cluster ClG 0217+70.
Methods. We observed ClG 0217+70 with LOFAR at 141 MHz and with VLA at 1.5 GHz, and we combined these observations with VLA 1.4 GHz archival data to study the morphological and spectral properties of the diffuse sources. We added *Chandra* archival data to examine the thermal and non-thermal properties of the halo.
Results. Our LOFAR and VLA data confirm the presence of a giant radio halo in the cluster centre and multiple relics in the outskirts. The radio and X-ray emission from the halo are correlated, implying a tight relation between the thermal and non-thermal components. The diffuse radio structure in the south-east, with a projected size of 3.5 Mpc, is the most extended radio relic detected to date. The spectral index across the relic width steepens towards the cluster centre, suggesting electron ageing in the post-shock regions. The shock Mach numbers for the relics derived from the spectral index map range between 2.0 and 3.2. However, the integrated spectral indices lead to increasingly high Mach numbers for the relics farther from the cluster centre. This discrepancy could be because the relation between injection and integrated spectra does not hold for distant shocks, suggesting that the cooling time for the radio-emitting electrons is longer than the crossing time of the shocks. The variations in the surface brightness of the relics and the low Mach numbers imply that the radio-emitting electrons are re-accelerated from fossil plasma that could originate in active galactic nuclei.

Key words. galaxies: clusters: individual: ClG 0217+70 – galaxies: clusters: intracluster medium – large-scale structure of Universe – radiation mechanisms: non-thermal – X-rays: galaxies: clusters

1. Introduction

Galaxy clusters reside at the intersection of cosmic filaments and grow through a series of mergers with smaller clusters or groups of galaxies. The merging of galaxy clusters (within a few gigayears) converts an enormous amount of gravitational energy (i.e. up to 10^{64} erg) into thermal and non-thermal energy. The thermal energy is produced by the heating and compression of the X-ray-emitting intra-cluster medium (ICM). The non-thermal energy is channelled through the acceleration of cosmic rays (CRs) and the amplification of large-scale magnetic fields. These events are the most energetic events in the Universe after the Big Bang (Sarazin 2002). During the mergers, shock waves and turbulence are generated in the ICM and are traced by diffuse radio synchrotron sources, namely radio halos and relics, respectively (see van Weeren et al. 2019 and Brunetti & Jones 2014 for recent reviews). Radio halos are steep-spectrum[1] ($\alpha \lesssim -1$), unpolarised, megaparsec-scale sources that are detected at the cluster centre, whereas radio relics are steep-spectrum, elongated sources that are highly polarised at gigahertz frequencies and are normally detected in the cluster outskirts.

The favoured model for the formation of halos is the turbulent re-acceleration model, in which fossil relativistic electrons ($\gamma \sim 10^2$ prior to the re-acceleration) in the cluster magnetic fields are re-accelerated by turbulence generated during mergers and, subsequently, emit synchrotron radiation (Brunetti et al. 2001; Petrosian 2001; Brunetti & Lazarian 2007, 2011, 2016; Pinzke et al. 2017). The relativistic electrons in relics were thought to be accelerated directly from the thermal pool at

★ A copy of the reduced images is only available at the CDS via anonymous ftp to cdsarc.u-strasbg.fr (130.79.128.5) or via http://cdsarc.u-strasbg.fr/viz-bin/cat/J/A+A/656/A154

[1] $S \propto \nu^{\alpha}$, where S is the flux density at frequency ν and α is the spectral index.

collisionless plasma shock fronts through *Fermi*-I diffusive shock acceleration (DSA; Bell 1978; Drury 1983; Blandford & Eichler 1987; Enßlin et al. 1998; Roettiger et al. 1999). Despite its success in explaining the observed properties of radio relics (i.e. morphological, spectral, and polarisation properties), the DSA model requires an unrealistically high acceleration efficiency to explain the observed surface brightness (SB) in some relics that are generated with low-Mach-number shocks (i.e. $\mathscr{M} \approx 1.5-3$) (e.g., Hoeft & Bruggen 2007; Vazza & Brüggen 2014; Botteon et al. 2020a). An alternative diffusive shock re-acceleration (DSRA) model, where a population of relativistic fossil plasma is required to be present prior to the re-acceleration by the passage of the low-Mach-number shocks, has been proposed to solve this energy problem (Markevitch et al. 2005; Kang & Ryu 2011; Kang et al. 2012). There has been observational evidence for this re-acceleration scenario in some clusters (e.g., van Weeren et al. 2013; Bonafede et al. 2014; Shimwell et al. 2015; Botteon et al. 2016; van Weeren et al. 2017; Hoang et al. 2018; Di Gennaro et al. 2018; Stuardi et al. 2019).

The galaxy cluster ClG0217+70 (hereafter ClG0217; z = 0.18, Zhang et al. 2020) was studied with the Very Large Array (VLA) at 1.4 GHz and 325 MHz by Brown et al. (2011) following its first detection with the Westerbork Northern Sky Survey (WENSS; Rengelink et al. 1997; Delain & Rudnick 2006; Rudnick et al. 2006). Brown et al. (2011) found that the cluster hosts multiple diffuse radio sources, including a radio halo in the cluster centre and multiple relics on opposite sides of the cluster and internal filaments. The presence of these diffuse radio sources is consistent with the picture that the cluster is dynamically disturbed, as is suggested by the elongating morphology of the X-ray emission in the ROSAT All-Sky Survey (RASS) image (Brown et al. 2011).

Brown et al. (2011) also analysed the photometric redshifts from galaxies in the field using Sloan Digital Sky Survey (SDSS) optical data and found that the cluster has a redshift of z = 0.0655, but they also suggested the need for deeper optical data to verify the result. With this low-redshift estimate, Brown et al. (2011) pointed out that the power of the radio halo in ClG0217 is an order of magnitude higher than the value predicted from the radio power–X-ray luminosity correlation (Liang et al. 2000; Cassano et al. 2006; Brunetti et al. 2009). However, recent work by Zhang et al. (2020) estimated a significantly higher redshift for the cluster (i.e. z = 0.18) from the Fe xxv Heα X-ray emission line that they detected in *Chandra* archival data. Using this new redshift, they found that the 1.4 GHz power of the radio halo and the 0.1–2.4 keV X-ray luminosity within R_{500}[2] are consistent with the radio power–X-ray luminosity relation.

The mass of ClG0217 is $M_{500} = (1.06 \pm 0.11) \times 10^{15}\, M_{\odot}$, estimated using the $M_{500} - kT$ scaling relation (Arnaud et al. 2007), making it one of the most massive clusters known. At the locations of the northern and southern radio halo edges (see Fig. 1 of Zhang et al. 2020), X-ray SB discontinuities with density jumps of $C_{\rm N} = 1.40 \pm 0.16$ and $C_{\rm S} = 3.0 \pm 0.6$, respectively, were found (Zhang et al. 2020). The radio emission at 1.4 GHz is found to rapidly steepen at the location of the northern X-ray SB jump towards the north. Due to the low integration time of the X-ray observations, it is not clear whether the discontinuities are caused by shocks or cold fronts.

In this paper we present LOw Frequency ARray (LOFAR; van Haarlem et al. 2013) 120–168 MHz and VLA 1–2 GHz (C-array) observations of ClG0217 to study the diffuse radio emission from the cluster. We combined the data with the VLA 1.37–1.48 GHz (D-array) archival data to examine the spectral properties of these sources. We did not include the relatively shallow VLA *P*-band data reported in Brown et al. (2011) in this study. In addition, *Chandra* X-ray archival data were used to examine the correlation between X-ray thermal and radio non-thermal emission from the radio halo. Throughout the paper, we assume a Lambda cold dark matter cosmology, with $\Omega_M = 0.3$, $\Omega_\Lambda = 0.7$, and $H_0 = 70\,{\rm km\,s^{-1}\,Mpc^{-1}}$. At the cluster redshift (z = 0.18), an angular scale of 1′ corresponds to a physical size of 182 kpc.

2. Observations and data reduction

2.1. LOFAR data

LOFAR High Band Antenna (HBA) observations of ClG0217 were performed for 8 hours on September 26, 2018 (project code: LC10_021). The observational settings are identical to those used by the LOFAR Two-metre Sky Survey (LoTSS; Shimwell et al. 2017, 2019). The 8-hour observation of the target field was book-ended by 10-minute scans of calibrators (i.e. 3C 196 and 3C 48). The observations were performed with core and remote stations in the Netherlands and international stations in surrounding European countries. The distances between the Dutch stations that are used in this study range from 42 m to 115 km, corresponding to 20 λ to 61 $k\lambda$ at the central frequency of 141 MHz. The high density of the LOFAR core stations makes it highly sensitive to diffuse sources. Details of the observations are given in Table 1.

The calibration of the LOFAR data was performed using the standard pipelines (i.e. `Prefactor`[3] and `DDF – pipeline`[4]) that have been developed for the LOFAR Surveys Key Science Project (van Weeren et al. 2016b; Shimwell et al. 2017, 2019; de Gasperin et al. 2019; Tasse et al. 2021). The pipelines address the direction-dependent and direction-independent effects that are commonly known to affect low-frequency radio observations. Following the direction-dependent calibration, all sources outside a square region of $1 \times 1\,{\rm deg}^2$ centred on the cluster were subtracted from the *uv* data. These subtracted data were then processed through several iterations of self-calibration to refine the image quality at the location of the target (van Weeren et al. 2021). We note that the data were applied an approximate correction for the LOFAR primary beam attenuation by multiplication with a factor during the subtraction step. However, as the pointing position is at the location of the cluster, the factor is 1. Due to the large angular distance of the sources to the pointing centre of ClG0217 (i.e. up to 15′), the flux densities of these sources were not properly corrected. We applied the primary beam correction during the final imaging steps below. To enhance faint, diffuse emission in the final images, we applied Briggs' weightings of the *uv* data using various `robust` values with `WSCLEAN` (version 2.9.3; Offringa et al. 2014; Offringa & Smirnov 2017). The imaging parameters are presented in Table 2. We also used joined-channel and multi-scale deconvolution (Offringa & Smirnov 2017) with the `join-channels` (`channels-out`=6) and `multiscale` (`multiscale-scales`=[0, 3, 7, 25, 60, 150]) options. The built-in option `apply-primary-beam` was added in the `CLEAN` command to correct for the response of the LOFAR primary beam across the imaged region.

[2] R_n is the radius in which the integrated mean density of the cluster is n times the critical density of the Universe at the cluster redshift.

[3] https://www.astron.nl/citt/prefactor

[4] https://github.com/mhardcastle/ddf-pipeline

Table 1. Observation details.

Telescope	LOFAR 141 MHz	VLA 1.4 GHz	VLA 1.5 GHz
Project	LC10_021	AD509	17A-083
Configuration	HBA_DUAL_INNER	D	C
Pointing position (RA, Dec)	$02^h17^m1.4^s$, $+70^d36^m16.0^s$	$02^h17^m0.0^s$, $+70^d36^m36.0^s$	$02^h18^m49.9^s$, $+70^d27^m36.0^s$ (E); $02^h14^m31.0^s$, $+70^d41^m04.0^s$ (W)
Observing dates	2018 Sept. 26	2005 Dec. 4, Dec. 8, Dec. 12	2017 Jun. 3
Obs. IDs	L670298	–	–
Calibrator(s)	3C 196	3C 286, 3C 352, 0217+738	3C 138, J0217+7349
Frequency (GHz)	0.120–0.168	1.37–1.48	1.008–2.032
Number of subbands	243	–	16
Bandwidth per subband (kHz)	195.3	–	64000
Channels per subband	16	–	64
On-source time (h)	8	3.5	1.7 (E) + 1.7 (W)
Integration time (s)	1	13	5
Frequency resolution (kHz)	12.2	12.5	1000
Correlations	XX, XY, YX, YY	RR, LL	RR, RL, LR, LL
Number of stations/antennas	60	23	27

We examine the flux scale of the LOFAR images by comparing the flux densities of compact sources in our LOFAR images with those detected with the TIFR Giant Metrewave Radio Telescope (GMRT) 150 MHz Sky Survey-Alternative Data Release (TGSS-ADR1; Intema et al. 2017). We selected compact sources that are brighter than 100 mJy and were detected with both the LOFAR and TGSS-ADR1 observations. The average flux densities for these sources in our LOFAR image are about 5 percent higher than those in the TGSS-ADR1 image. In this paper, we adopt a flux scale uncertainty of 10 percent on the LOFAR data as assumed by a number of previous studies (e.g., Bruno et al. 2021; Rajpurohit et al. 2021a).

2.2. VLA data

We observed ClG0217 with the VLA *L*-band (1.5 GHz) in C array on June 3, 2017 (Project: 17A-083) and combine with archival data obtained with the VLA *L*-band (1.4 GHz) D array between December 4 and 12, 2005 (Project: AD509). Details of these observations are summarised in Table 1.

The VLA *L*-band C-array observations were performed using two pointings centred 13′ to the north-west and to the south-east of the centre of the cluster. This was done to increase the sensitivity to the sources in the peripheral regions of the cluster. We processed the data using the VLA `CASA` calibration pipeline version 4.7.2. The processing was optimised with the additional flagging and calibration to produce high-quality images. 3C 138 was used as amplitude and bandpass calibrator; and J0217+7349 was used for a phase calibration. After the initial imaging, several cycles of self-calibration were separately performed on the two pointings in order to refine the calibration. Finally, we make use of the `tclean` task in `CASA` (version 5.6; McMullin et al. 2007) to separately make intensity images for two pointings. A wideband correction for the primary beam attenuation using the `widebandpbcor` task was applied to the images. We then combined the images to make a mosaic of the cluster. The pixel values in the overlay regions between the pointings where the amplitude of the primary beams are larger than 0.2 were averaged, weighted by their amplitude.

We reprocessed the VLA *L*-band D-array datasets that were originally presented in Brown et al. (2011). The data were calibrated using `CASA` (version 5.6; McMullin et al. 2007). The flux densities of the sources are calibrated using observations of 3C 286 and 3C 352 that we tied to the Perley & Butler (2017) flux scale. The compact source 0217+738, which is located approximately 3 degree from ClG0217, was observed in-between target scans and was used as a phase calibrator. The calibration was performed for each dataset in a standard manner (i.e. flagging of outliers, calibrating of the flux scale, antenna position, phase delay, bandpass, and complex gain). After the initial calibration, the datasets were combined and processed through multiple loops of self-calibration. The final, calibrated data were used to make an image of the cluster using Briggs' weighting (see Table 2). The final image was also corrected for the attenuation of the primary beam (i.e. by using `pbcor=True` option in `tclean`). We adopted a flux scale uncertainty of 5 percent associated with the calibration of the VLA data. Due to the different settings (i.e. pointing positions) of the VLA C-array and D-array observations, we do not combine the datasets for final imaging.

2.3. Removal of discrete sources

The diffuse sources in ClG0217 are contaminated by discrete sources, which we removed from the LOFAR and VLA D-array *uv* data by subtracting their models. The removal of the discrete sources is essential for determining the flux density and spectra of the diffuse sources. To remove discrete sources, their source models at 141 MHz and 1.4 GHz were created by imaging the data at high resolutions using only the baselines longer than 2 kλ (i.e. corresponding to an angular size of smaller than 2.1′ or 382 kpc at $z = 0.18$) and applying Briggs' weighting to give more weight to the long baselines (i.e. `robust` = −0.25 for LOFAR and `robust` = −2 for VLA). An advantage of the combination of these settings is that they prevented any significant large-scale emission from being present in the model images, which is subtracted from the data. Moreover, when including more data for imaging, the noise level of the model images is lowered, which allows the detection of faint, compact sources. In Appendix A we present the LOFAR and VLA high-resolution images that are obtained with these tuned imaging parameters. The discrete sources are identified with `PyBDSF` using a source detection threshold of 4σ (i.e. `thresh_pix` = 4). These

Table 2. Imaging parameters.

Data	uv-range [kλ]	Robust [(a)]	uvtaper [″]	θ_{FWHM} [″×″], (PA [(b)][°])	$\sigma_{\rm rms}$ [μJy beam^{-1}]	Figure
LOFAR	0.12 – 61	0	5	14.6 × 10.1 (−85)	160	1
	0.12–61	0	15	26.6 × 22.5 (29)	240	4
	0.12–61	0.25	25	45.7 × 44.7 (52)	335	3
	0.12–61	0	5	16 × 16 [(c)]	190	6 [(d)]
	0.12–61	0	30	46 × 46 [(c)]	345	6 [(d)], 7 [(d)], 9
	2–61	−0.25	5	11.2 × 7.5 (−89)	140	A.1 [(e)]
VLA (C-array)	0.12–22	0	8	16 × 16 [(c)]	40	2, 6 [(d)]
VLA (D-array)	0.12–5.1	0	–	46 × 46 [(c)]	85	2, 6 [(d)], 7 [(d)], 9 [(d)]
	2.0–5.1	−2	–	28.4 × 24.6 (51)	80	A.1 [(e)]

Notes. [(a)]Briggs weighting, [(b)]PA: position angle with the reference axis to the N and anticlockwise as positive, [(c)]smoothed, [(d)]spectral index, [(e)]beam uncorrected.

clean-component models of the contaminating sources were then subtracted from the LOFAR and VLA uv data.

2.4. Spectral index maps

We combined the LOFAR 141 MHz data with the VLA 1.4 GHz (D-array) and 1.5 GHz (C-array) data to make spectral index maps of the radio sources in the cluster field. When making the LOFAR and VLA intensity images, we selected the uv data with a common inner uv cut for both datasets. Here we used an inner uv cut of 0.12 $k\lambda$ for the 16″ and 46″ resolution maps. Briggs' weighting of the uv data (`robust` = 0) is combined with tapering of the outer baselines (`uvtaper`) to obtain images with the resolutions that are close to the targeted resolutions (i.e. 16″ and 46″). The imaging of the LOFAR and VLA data were done with `WSClean` and `CASA`, respectively (see Sects. 2.1 and 2.2). The LOFAR and VLA images were smoothed to the final resolutions, aligned using compact sources, and re-gridded to the same pixel size. The properties of the final images are given in Table 2. Spectral index maps were made with the LOFAR and VLA final images, following the power-law relation of the synchrotron spectrum ($S \propto \nu^{\alpha}$). The spectral index errors are added in quadrature from the flux scale uncertainty and the image noise.

2.5. Chandra data

The *Chandra* observations of ClG0217 using the Advanced CCD Imaging Spectrometer (ACIS) were performed for 25 ks on November 28, 2014 (ObsID: 16293). The calibration of the data was done in Zhang et al. (2020). For completeness, we briefly describe it here. The level-2 event files were obtained with the *Chandra* Interactive Analysis Observations (CIAO)[5] package using the `chandra_repro` task. The X-ray SB image in the energy band 1−3 keV was extracted with the `fluximage` task. The SB image was then subtracted from the non-X-ray background (NXB), corrected for the vignetting, and adaptively smoothed.

3. Results and analysis

In Fig. 1 we present our deep LOFAR 141 MHz 14.6″ × 10.1″ resolution image of the galaxy cluster ClG0217. For the first time, the LOFAR observations allowed us to image the cluster at a frequency below 350 MHz.

We have labelled the sources following Brown et al. (2011) and split sources B and E from Brown et al. (2011) into separate sources, B1+B2 and E1+E2. We have also added sources C1 and F1, which are newly detected with the LOFAR observations. The VLA C- (1.5 GHz) and D-array (1.4 GHz) images are shown in Fig. 2. The LOFAR 141 MHz and VLA 1.5 GHz images confirm the presence of central halo emission (A) and several elongated diffuse radio sources (C, D, E1+E2, F, and G) in the outskirts, detected previously at 1.4 GHz by Brown et al. (2011). In the subsections below, we present the flux density and spectral measurements of the diffuse sources in the cluster and summarise the results in Table 3.

3.1. Central radio halo

As shown in Figs. 1 and 2, the radio halo has a fairly round shape. The largest linear size (projected) of the halo is about 1.8 Mpc and 1.5 Mpc at 141 MHz and 1.4 GHz (measured from the D-array image), respectively. Apparently, the sensitive low-frequency observations allow us to reveal more extended very low SB emission. In the new VLA C-array image in Fig. 2 (*left*), the halo size is significantly smaller (i.e. 800 kpc). This is likely due to the fact that the VLA C-array observations lack the sensitivity (i.e. signal-to-noise ratio) to the large-scale (i.e. ∼10′ of the halo) emission, although the largest angular detectable scale of the C array[6] is 16′.

The morphology of the halo emission is similar at 141 MHz and 1.4 GHz. Figure 1 shows some substructures within the halo emission at 141 MHz. Multiple unrelated discrete sources are also embedded in the southern and northern regions of the halo.

The low-resolution (45.7″ × 44.7″), point-source-subtracted LOFAR image of the halo superimposed on the *Chandra* X-ray contours is shown in Fig. 3. As typical for halos, the radio emission from the halo seems to follow the thermal X-ray emission, implying a connection between the thermal and non-thermal components of the ICM.

Interestingly, Fig. 3 also shows that the southern and eastern regions of the halo are apparently connected to elongated diffuse sources D and E2, respectively. The connection between the halo

[5] https://cxc.harvard.edu/ciao

[6] https://science.nrao.edu/facilities/vla/docs/manuals/oss2017A/performance/resolution

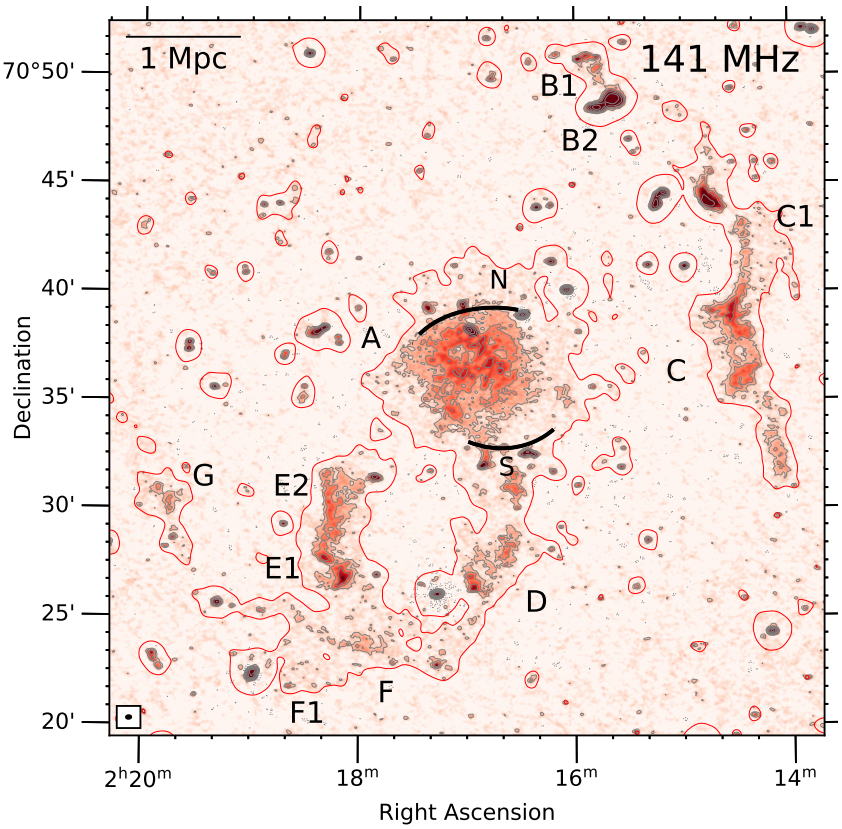

Fig. 1. LOFAR 14.6″ × 10.1″ resolution image of the galaxy cluster ClG0217. The image shows the roundish halo emission (A) at the cluster centre and relics (C, D, F, and G) in the outskirts. The first grey contour starts from 3σ, where $\sigma = 160\,\mu\mathrm{Jy\,beam^{-1}}$. The subsequent contours are multiplied by a factor of two. The red contour level is 3σ, where $\sigma = 335\,\mu\mathrm{Jy\,beam^{-1}}$ with a beam size of 45.7″ × 44.7″. The synthesised beam of 14.6″ × 10.1″ is shown in the bottom-left corner. The arc lines show the locations of detected X-ray SB discontinuities in the northern and southern edges of the halo that are found in Zhang et al. (2020).

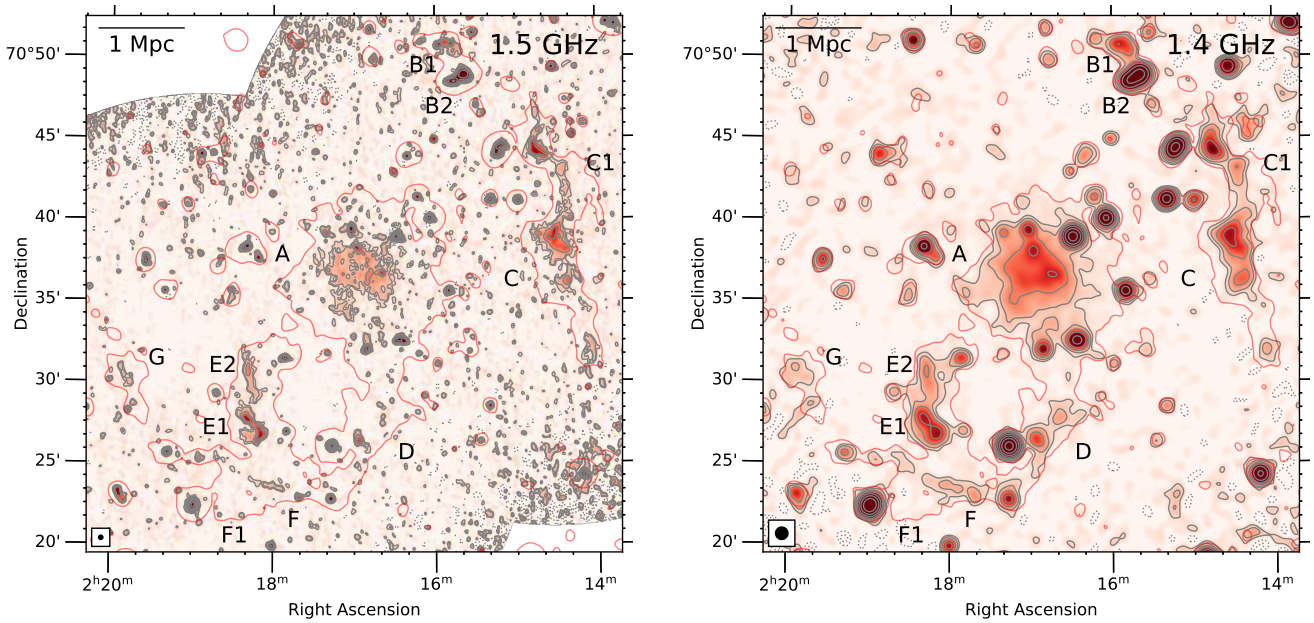

Fig. 2. VLA C- (*left*) and D-array (*right*) images. The contour starts from 3σ, where $\sigma_{\mathrm{C-array}} = 40\,\mu\mathrm{Jy\,beam^{-1}}$ and $\sigma_{\mathrm{D-array}} = 85\,\mu\mathrm{Jy\,beam^{-1}}$. The subsequent contours are multiplied by a factor of two. The synthesised beams are drawn in the bottom-left corners (i.e. 16″ × 16″ for the C-array image and 46″ × 46″ for the D-array image). The LOFAR 45.7″ × 44.7″ resolution contour is the same as that in Fig. 1.

and sources D and E2 can only be seen at 141 MHz, suggesting that these regions have steep spectra ($\alpha < -1.6$).

3.1.1. Flux density and radio power

The 141 MHz flux density of the radio halo measured within the 3σ contour of the discrete-source-subtracted image is 597.7 ± 59.9 mJy. In Fig. 4 we show the low-resolution image and the regions used for extracting the halo flux density. The measured halo flux density increases by 2.6 percent to 613.4 ± 61.5 mJy when all pixels above 2σ are included. At 1.4 GHz, we measure the flux density for the halo integrating over the 3σ and 2σ regions to be 46.9 ± 2.5 mJy and 51.1 ± 2.7 mJy (a 9.0 percent increase), respectively. Using the same VLA datasets, Brown et al. (2011) reported a higher value (i.e. 58.6 ± 0.9 mJy or ∼15 percent higher than our 2σ measurement). It is

Table 3. Radio source properties.

Source	$S_{141\,\mathrm{MHz}}$ [a] [mJy]	$P_{141\,\mathrm{MHz}}$ [b] [10^{24} W Hz^{-1}]	$S_{1.4\,\mathrm{GHz}}$ [a] [mJy]	$P_{1.4\,\mathrm{GHz}}$ [b] [10^{23} W Hz^{-1}]	α	LAS [c] [Mpc]
A	613.4 ± 61.5	56.4 ± 5.7	51.1 ± 2.7	47.0 ± 2.5	−1.07 ± 0.05	1.8
	623.6 ± 62.7 [d]	56.9 ± 5.7 [d]	58.3 ± 3.4 [d]	53.2 ± 3.1 [d]	−1.02 ± 0.05 [d]	–
B1	24.6 ± 2.6	2.1 ± 0.2	5.2 ± 0.3	4.5 ± 0.3	−0.67 ± 0.05	0.3
B2	170.3 ± 17.1	15.1 ± 1.5	23.5 ± 1.2	2.1 ± 0.1	−0.86 ± 0.05	–
C	211.4 ± 21.3	19.3 ± 2.0	20.3 ± 1.1	18.5 ± 1.0	−1.01 ± 0.05	2.3
C1	13.7 ± 1.8	1.3 ± 0.2	<0.3 [c]	<0.3	< −1.7	0.7
D	127.0 ± 13.0	12.3 ± 1.3	5.7 ± 0.5	5.5 ± 0.5	−1.34 ± 0.06	1.8
E1	84.2 ± 8.5	7.6 ± 0.8	9.7 ± 0.6	8.7 ± 0.5	−0.93 ± 0.05	0.5
E2	93.3 ± 9.5	8.8 ± 0.9	5.9 ± 0.4	5.5 ± 0.4	−1.19 ± 0.05	1.0
F	59.8 ± 6.3	5.5 ± 0.6	4.8 ± 0.4	4.4 ± 0.4	−1.09 ± 0.06	1.7
F1	15.1 ± 1.8	1.6 ± 0.2	<0.3 [c]	<0.3	< −1.7	0.6
G	31.4 ± 3.5	2.9 ± 0.3	3.1 ± 0.3	2.8 ± 0.3	−1.00 ± 0.06	1.6

Notes. [a]The flux density is calculated for all pixels that are detected above 2σ, except in the case of [d], where flux density is obtained by fitting the SB of the halo with a two-dimensional circular model. [b]k-corrected radio power, $P = 4\pi D_L^2 S_\nu/(1+z)^{(1+\alpha)}$, where D_L is the luminosity distance. [c]Largest angular size. [d]Upper limit estimated by $\sigma \times \sqrt{N}$, where N is the source area in beam unit.

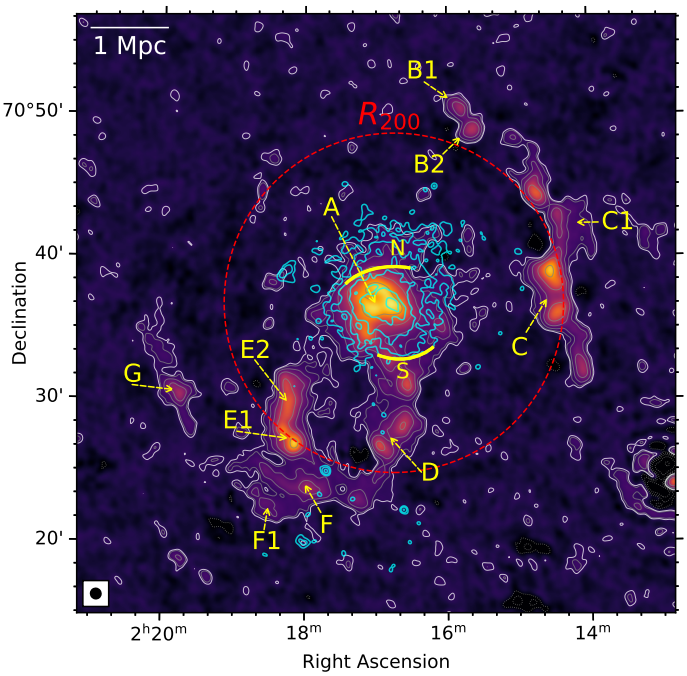

Fig. 3. LOFAR 45.7″ × 44.7″ resolution image of ClG0217. The contaminating discrete sources are removed from the data. The LOFAR grey and *Chandra* cyan contours are drawn at $\pm[1, 2, 4, 8, 16] \times 3\sigma$, where $\sigma_{\mathrm{LOFAR}} = 335\,\mu\mathrm{Jy\,beam^{-1}}$ and $\sigma_{Chandra} = 1.3 \times 10^{-6}$ cts arcmin^{-2} cm^{-2}. The LOFAR white contour is drawn at $2\sigma_{\mathrm{LOFAR}}$. The *Chandra* data are smoothed with a Gaussian beam of five-pixel sigma, where pixel size is 1.968″. The dashed red circle has a radius of $R_{200} = 2.3$ Mpc. The arc lines show the locations of the northern and southern X-ray SB discontinuities.

unclear where this difference comes from. It could be due to the differences in the thresholds and/or the absolute flux scale that are not described in Brown et al. (2011). The deconvolution algorithms might also contribute to the difference in the flux density reported in this work and Brown et al. (2011).

The application of a threshold cut to the pixel values used when integrating the halo flux might bias the measurement low, due to missing flux from the faint emission in the outer regions of the radio halo. For comparison and better recovery of the low-SB emission, we fitted the SB of the halo with a two-dimensional circular exponential model of the form

$$I(r) = I_0 \exp(-r/r_e), \tag{1}$$

where the fitting parameters I_0 and r_e are the SB at the halo centre and the e-folding radius, respectively (Murgia et al. 2009). We made use of the `Halo-FDCA`[7] code (Boxelaar et al. 2021) that has been used to estimate the flux densities of the radio halos detected in the HETDEX (Hobby-Eberly Telescope Dark Energy Experiment) field of the LoTSS survey (van Weeren et al. 2021). The code employs a Markov chain Monte Carlo (MCMC) method to search for the best-fit parameters and the associated uncertainties. In the halo of ClG0217, we find the best-fit parameters to be $I_0 = 15.51 \pm 0.18\,\mu\mathrm{Jy\,arcsec^{-2}}$ and $r_e = 255 \pm 2$ kpc at 141 MHz and $I_0 = 1.19 \pm 0.04\,\mu\mathrm{Jy\,arcsec^{-2}}$ and $r_e = 281 \pm 7$ kpc at 1.4 GHz. The corner plots showing the constraints of the fitting are presented in Appendix B. The e–folding radius at 1.4 GHz is larger than that at 141 MHz, indicating the full extent is not detected with the current shallow data. Alternatively, the fitting might be biased by possible excess radio emission in the outer regions of the halo at 1.4 GHz that is associated with X-ray SB discontinuities to the northern, southern and north-eastern regions (discussed in Sect. 3.1.3).

Using the best fit parameters, the flux density is integrated to a defined radius. The flux density for the halo in ClG2017 is 623.6 ± 62.7 mJy at 141 MHz and 58.3 ± 3.4 mJy at 1.4 GHz. The flux density above is integrated up to a radius of $4r_e$, which is slightly larger than the half of the halo size (i.e. 900 kpc) within the 2σ contours. This consists of 90 percent of the flux density when integrating to infinity. In order to obtain the total errors in the flux density, the uncertainties associated with the model fitting and the LOFAR and VLA flux calibration (i.e. 10% and 5%, respectively) are added in quadrature. The corresponding k-corrected radio power for the radio halo is $56.9 \pm 5.7 \times 10^{24}$ W Hz^{-1} at 141 MHz and is $53.2 \pm 3.1 \times 10^{23}$ W Hz^{-1} at 1.4 GHz.

Finally, in Fig. 5 we show the radio power versus cluster mass relation of known halos. The radio power of the

[7] https://github.com/JortBox/Halo-FDCA

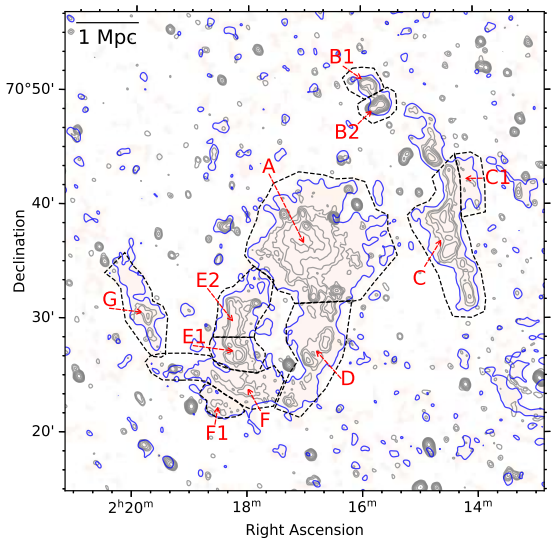

Fig. 4. LOFAR 26.6″ × 22.5″ resolution image. The contour levels are the same as those in Fig. 1 with $\sigma = 240\,\mu\mathrm{Jy\,beam^{-1}}$. The blue compact-source-subtracted contour is drawn at 2σ, where $\sigma = 335\,\mu\mathrm{Jy\,beam^{-1}}$ and the beam size is 45.7″ × 44.7″. The dashed black lines show the regions used to measure the flux densities from the diffuse cluster sources, and the measurements are summarised in Table 3.

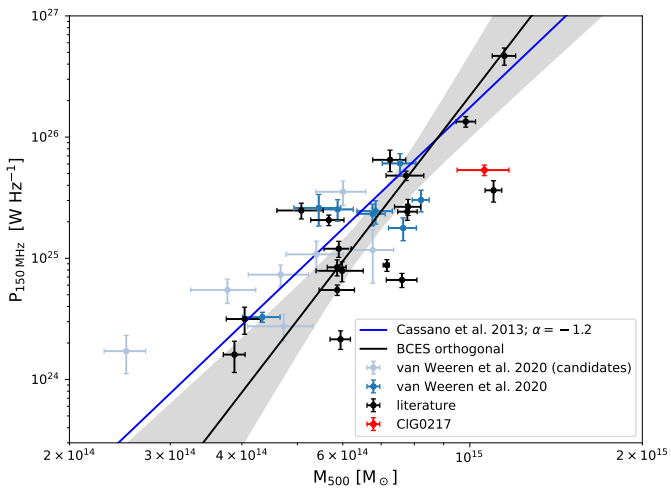

Fig. 5. $P_{150\,\mathrm{MHz}} - M_{500}$ correlation, including the data point for the radio halo in ClG0217 (in red). The plot is adapted from van Weeren et al. (2021).

ClG0217 halo is a bit lower than expected from the correlation between radio power and cluster mass, even though one should note the large scatter of the data points around the scaling relation.

3.1.2. Spectral index measurements

Using the flux density estimates obtained from the exponential model fitting, we find that the integrated spectral index between 141 MHz and 1.4 GHz for the radio halo is −1.02 ± 0.05, which is consistent with the value of −1.07 ± 0.05 that is obtained using the measurements from the 2σ threshold cut method. When combining our measurements with the 325 MHz flux density reported in Brown et al. (2011), we obtain integrated spectral indices of −0.78 ± 0.16 between 141 MHz and 325 MHz and −1.16 ± 0.07 between 325 MHz and 1.4 GHz. This implies that the radio halo has a curved spectrum with steeper index at high frequencies. However, we also note that the 325 MHz observations have a resolution too low to resolve the compact sources to the northern edge of the halo, as seen in Fig. 2 of Brown et al. (2011). These compact sources might contaminate the flux measurement at 325 MHz, making the halo spectra deviate from its true values. We estimate that the halo follows a simple power-law spectrum if 20 percent of its 325 MHz flux density is subtracted due to the possible contamination by the compact sources.

In Fig. 6 we show the low-resolution (46″) spectral index map of ClG0217 that was made with the LOFAR 141 MHz and VLA 1.4 GHz data. The cutout images show the distribution of the spectral index in the source regions at a resolution of 16″. The corresponding spectral index error maps are presented in Appendix C. In the central region of the halo, the spectral index remains roughly constant, but it seems to flatten in the outer regions. We note that the spectral index in the outermost regions of the halo might be contaminated by the imperfection of the subtraction of discrete sources.

To examine the radial spectral distribution of the halo, we extract the spectral index in circular annuli that have a width of 50″ (i.e. slightly larger than the beam size of 46″). These regions are shown in the left panel of Fig. 7. We note that, as mentioned in Sect. 2.3, the discrete sources were subtracted from both LOFAR and VLA images. The resulting radial spectral index profile that is shown in the right panel of Fig. 7 suggests a uniform spectral index of −1.07 ± 0.02 within a radius of 680 kpc (i.e. over an area of 1.5 Mpc^2). Although there is hint of radial spectral flattening within the radius of ∼600 kpc, the spectral trend is within the 1σ uncertainty. In the outer region ($r \geq 830$ kpc), the index becomes steeper than −1.14. We note that deeper radio observations are required to estimate the spectral index as the low SB emission in this region may not be fully deconvolved. The errors estimated in the profile do not include the uncertainty associated with the flux scale calibration as, if included, the spectral index is systematically rather than randomly impacted. However, if the flux scale uncertainty is added in quadrature with the image noise, the typical errors for the spectral indices are 0.06. Hence, this does not change our conclusion on the spectral index uniformity in the central region of the radio halo.

3.1.3. The north-eastern edge

A recent study by Zhang et al. (2020) found discontinuities in the X-ray SB towards the northern and southern edges of the radio halo in the VLA 1.4 GHz data. The locations of these discontinuities are also shown in Fig. 3. In addition to these two edges, we note that the north-eastern edge of the radio halo in the LOFAR 141 MHz map could be associated with a new X-ray SB discontinuity. To examine this possibility, we extract a *Chandra* SB profile using the box regions defined in the inset of Fig. 8. The resulting profile is shown in Fig. 8. We fit the X-ray data using a projected broken power-law density model (Owers et al. 2009) and obtained a best-fit density jump of 1.92 ± 0.34 at the radius of 195″ ± 8″. Meanwhile, we extract the radio SB profile in this region from the 46″ resolution map. The radio profile nicely follows the trend of the X-ray SB before the jump and drops quickly at the X-ray SB jump. The five outermost radio data points below $1.5\sigma_{\mathrm{rms}}$ are regarded as the radio background. The new north-eastern X-ray edge partly overlaps with the previously reported northern edge in Zhang et al. (2020).

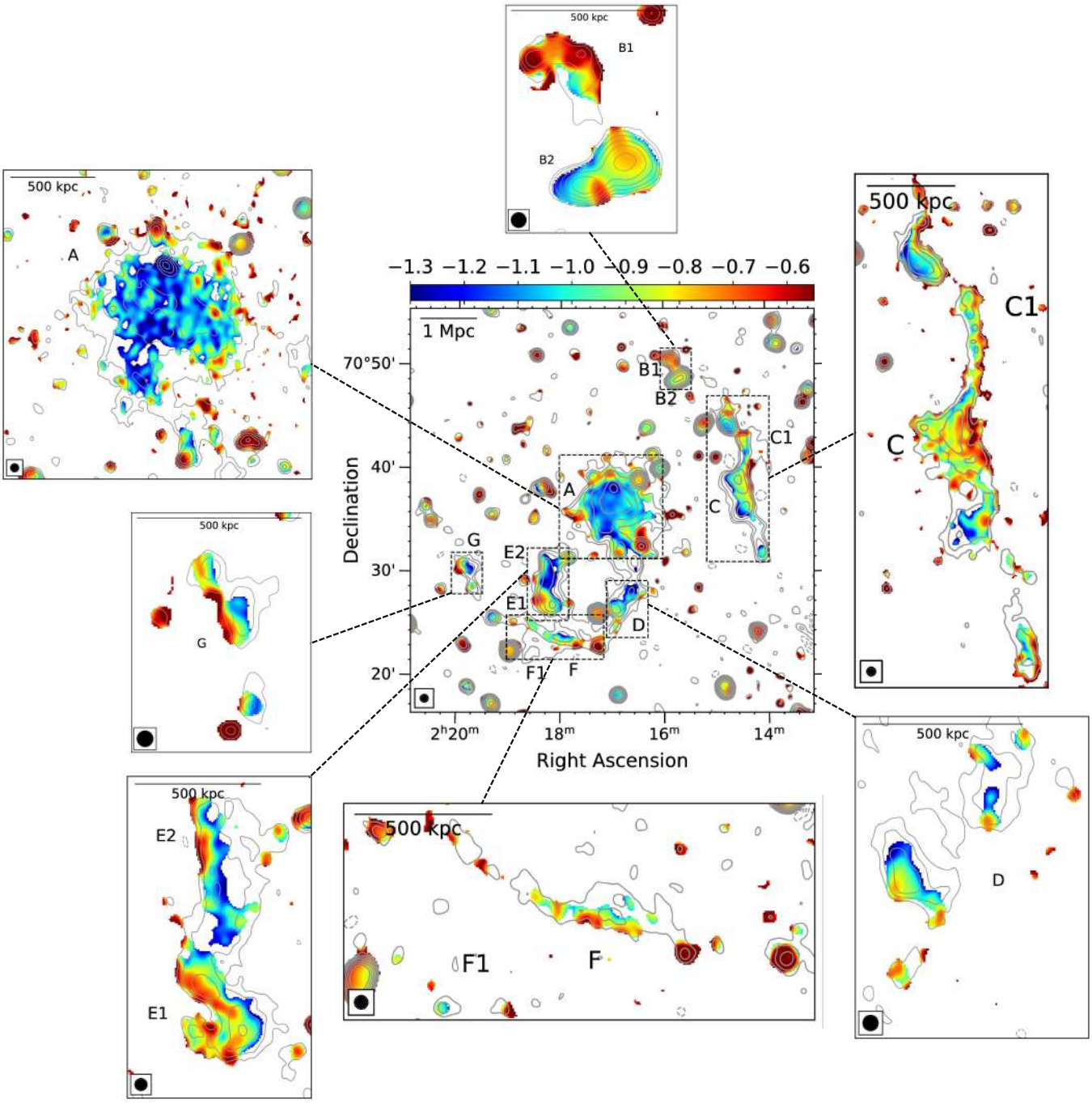

Fig. 6. Spectral index map (central) between 141 MHz and 1.4 GHz at the resolution of 46″. The cutout images show the distribution of spectral indices between 141 MHz and 1.5 GHz at 16″ resolution. The LOFAR contour levels are $\pm[1, 2, 4, 8, 16] \times 3\sigma$, where $\sigma = 345\,\mu\mathrm{Jy\,beam^{-1}}$ ($\mathrm{beam}_{FWHM} = 46''$) and $\sigma = 190\,\mu\mathrm{Jy\,beam^{-1}}$ ($\mathrm{beam}_{\mathrm{FWHM}} = 16''$) for the central and the cutout images, respectively. The corresponding maps for the spectral index errors are presented in Appendix C.

Although the nature of the X-ray SB discontinuities is still unknown and the relation between the north and the north-eastern discontinuities is unclear yet, if they have a nature of a shock front, they might affect the spectra of the non-thermal emission in the regions. We examine the spectral index trend towards the northern and southern regions of the halo using the 46″ resolution spectral index image. The spectral indices are extracted from the northern and southern sectors shown in the left panel of Fig. 7. The width of the radial sub-regions is taken to be approximately the size of the synthesised beam (i.e. 48″ and 53″ for the northern and southern sectors, respectively). The corresponding spectral index profiles in the right panel of Fig. 7 show that the spectral index does not change (i.e. within 1σ) towards the directions of the X-ray SB jumps. This might be because the spectral index map with the resolution of 46″ (140 kpc) cannot resolve the spatial spectral structure of the diffuse radio emission in this region of the halo. Although there are hints of a spectral flattening towards the regions of the X-ray SB jumps, high uncertainties in the spectral index measurements prevent us from drawing a conclusion from the trend. Future deep, high-resolution radio observations will be necessary.

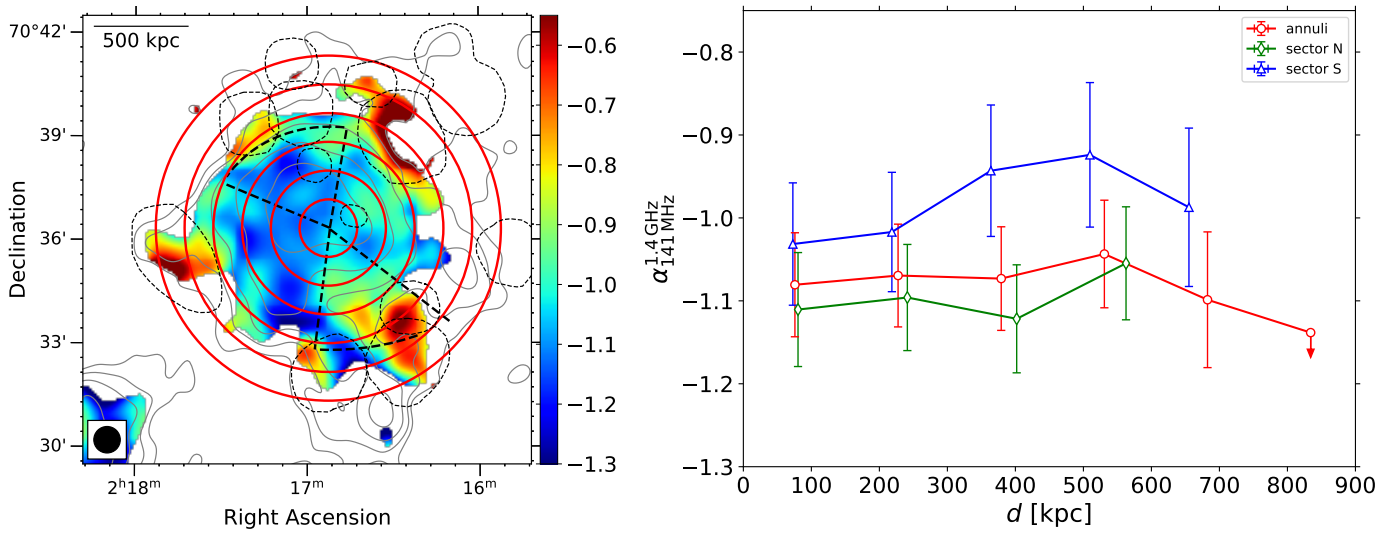

Fig. 7. *Left*: 141 MHz–1.4 GHz spectral index map in the halo region. The discrete sources were removed from the data before the spectral index map was made. The red annuli and black dashed sectors are where the spectral indices are estimated, and they are shown in the right panel. The outermost regions of the N and S sectors are where X-ray SB discontinuities are found in Zhang et al. (2020). The thin dashed lines are the regions where discrete sources are subtracted or show locally flat spectra, which are excluded from the profiles. The LOFAR grey contours are $\pm[1, 2, 4, 8, 16] \times 3\sigma$, where $\sigma = 345$ μJy beam^{-1} (beam$_{FWHM}$ = 46″). *Right*: spectral index profiles from the halo centre towards the outskirts and towards the N and S sectors.

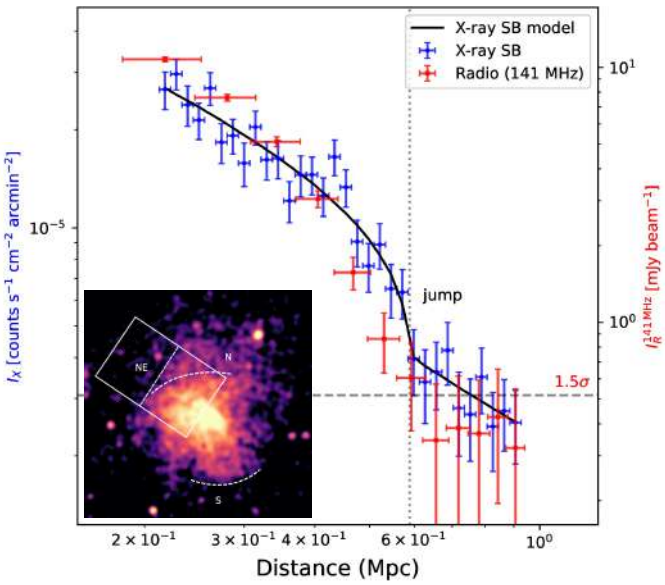

Fig. 8. X-ray and radio (141 MHz) SB profiles towards the north-east direction of the halo. The X-ray SB model indicates a discontinuity, which is marked by the vertical dotted line. In the overlaid *Chandra* image, the extracted north-eastern region is shown with the rectangles. The dashed N and S arcs are the X-ray SB edges found by Zhang et al. (2020).

3.1.4. Radio and X-ray SB correlation

With the current data, the X-ray emission from the ICM of ClG0217 is approximately as extended as the size of the radio emission, as seen in Fig. 3. It is noted that the *Chandra* data were obtained from the shallow 25 ks observations that might not detect the faint emission in the outer region of the cluster. The intensity of the X-ray and radio diffuse emission in the halo region is spatially correlated. This is clearest in the central region of the halo where elongated sub-structures in the X-ray and radio emission are seen in the NE-SW direction.

The correlation between radio and X-ray emission in the cluster central region has been found to follow a power-law relation,

$$\log_{10} I_R = a + b \times \log_{10} I_X, \tag{2}$$

where a and b are free parameters (e.g., Govoni et al. 2001a,b; Feretti et al. 2001; Bruno et al. 2021; Rajpurohit et al. 2021a). The parameter b describes how the X-ray and radio SB are correlated. For $b = 1$, the SB of the thermal and non-thermal emission is linearly related over the source. Whereas, the SB values are sub-linearly and super-linearly related in cases of $b < 1$ and $b > 1$, respectively. In case of sub- or super-linear correlation, the non-thermal components radially decline slower or faster than the thermal ones.

We quantitatively examine the correlation between the thermal X-ray and non-thermal radio emission from the ClG0217 halo by performing a point-to-point analysis using the X-ray *Chandra* and radio images (i.e. LOFAR 141 MHz and VLA 1.4 GHz maps at 46″ resolution). We extract the X-ray and radio SB from 48 square regions that have sizes of 60″ × 60″ (i.e. 182 × 182 kpc^2), covering up to 1.5 Mpc^2 area of the halo. The grid used for extracting the X-ray and radio SB values is shown in the *left* panel of Fig. 9. The size of each square region is set to be larger than the size of the synthesised beam, which is 46″. We note that the regions are selected based on the LOFAR 2σ contours but exclude the flat spectral index regions that are likely to be affected by the imperfect subtraction of compact sources. The *Chandra* image is smoothed with a two-dimensional Gaussian function that has a kernel of five pixels (i.e. 5 × 1.968″).

In the middle panel of Fig. 9, we show the point-to-point relation between the radio and X-ray SB. To check if there exists any significant correlation between these two quantities, we fit the observed data with a Bayesian linear regression using the `linmix` package[8]. The `linmix` takes into account the

[8] https://github.com/jmeyers314/linmix

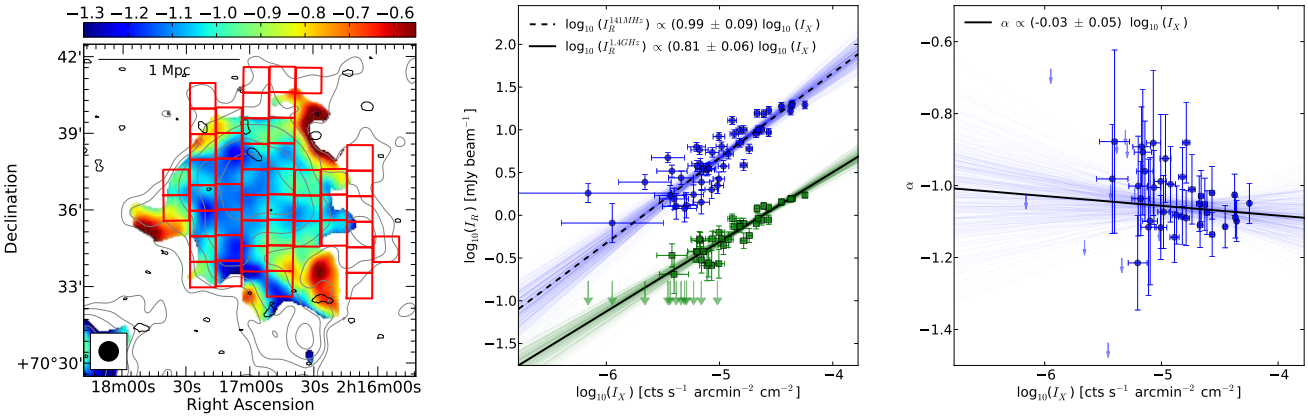

Fig. 9. *Left*: regions where radio and X-ray data are extracted. *Middle*: correlation between radio and X-ray SB. *Right*: scatter plot of the radio spectral index and X-ray SB. The solid and dashed (black) lines show the best-fit results from the MCMC runs. The thin (blue and green) lines are the fitting results of some individual MCMC runs. In both plots, the 2σ upper limits are shown with the downward- and leftward-pointing arrows.

Table 4. Parameters for the radio and X-ray SB correlation.

	b	r	D.o.F.	p
LOFAR	1.03 ± 0.09	0.91	43	<0.001
VLA	0.81 ± 0.06	0.97	34	<0.001
α	-0.02 ± 0.06	−0.21	34	0.20

uncertainties of both X-ray and radio data (Kelly 2007) and also non-detections. For the halo in ClG0217, we find a linear and sub-linear positive correlations at 141 MHz and 1.4 GHz, respectively. The correlation slope is $b_{141\,\mathrm{MHz}} = 1.03 \pm 0.09$ and $b_{1.4\,\mathrm{GHz}} = 0.81 \pm 0.06$. In Table 4, we report the Pearson's (linear) correlation coefficients (r), including the degree of freedom (d.o.f.) and the p value. The results suggest tight correlations between the radio and X-ray emission for the halo at both 141 MHz and 1.4 GHz. The obtained correlation slopes imply that the non-thermal components at 1.4 GHz decline more slowly than that at 141 MHz, which is in line with the tentative flattened trend in our spectral index radial profile within the radius of 600 kpc, as discussed in Sect. 3.1.2.

In a similar manner, we extracted the spectral indices in the square regions to study its relation with the X-ray SB that is fit with a relation of the form

$$\alpha = a + b \times \log_{10} I_X. \tag{3}$$

The resulting plot between the spectral indices and X-ray SB is shown in the right panel of Fig. 9. We obtained a slope of $b = -0.02 \pm 0.06$ and a Pearson's coefficient of $r = -0.21$, suggesting that the spectral index in the halo region is independent from the X-ray SB change. As the square regions in which the spectral indices are calculated are within a radius of 600 kpc, this result is in line with the spectral index profile shown in Fig. 7. We estimate the mean spectral index over the square regions in Fig. 9 (left) to be -1.03 ± 0.13, which is consistent within 1σ with the integrated spectral index for the halo (i.e. $\alpha = -1.07 \pm 0.05$).

3.2. Peripheral diffuse sources

The cluster ClG0217 is known to host several diffuse sources in the outskirts. Source C (for labelling, see Fig. 4), located at 15′ to the west of the cluster centre, was classified as a radio relic by Brown et al. (2011). The measured projected length of the relic is about 1.7 Mpc at 1.4 GHz. In our deep LOFAR images, relic C is 35 percent longer with a projected size of 2.3 Mpc. For these measurements, we do not include the bright, compact source to the north of the relic. A Panoramic Survey Telescope and Rapid Response System (Pan-STARRS; Flewelling et al. 2020) optical counterpart in the radio emission peak suggests that the radio emission to the north of the relic is originated from a radio galaxy. We present a Pan-STARRS image of the optical source overlaid with LOFAR contours to show the connection in Appendix D. At 141 MHz, the width of relic C in projection is about 620 kpc in the middle region, as shown in Fig. 3, and it gets narrower (i.e. 280 kpc) towards the south and north directions. In the north-western region of the relic, a diffuse, faint source, namely C1, is detected in the LOFAR low-resolution (45.7″ × 44.7″) image, but it is not seen in the VLA images, which are shown in Fig. 2. We estimate that the 141 MHz–1.4 GHz spectral index of C1 is steeper than −1.7.

For relic C, we measure a flux density at 141 MHz and 1.4 GHz within the LOFAR 2σ region and summarise these measurements in Table 3. The region used for the flux density measurement is shown in Fig. 4. Using these flux measurements, we estimate the integrated spectral index of relic C to be -1.01 ± 0.05 that is within typical range for known radio relics (e.g., van Weeren et al. 2019). However, this value is significantly flatter than that of C1, which may imply their different origins. In Fig. 6, relic C shows a clear spectral steepening in the downstream regions, towards the cluster centre. In the middle region, the spectral index decreases from −0.72 on the western side to −1.35 on the eastern side. We also extract the spectral index profile across relic C and present it in the right panel of Fig. 10. The spectral indices are estimated within the 46″-width regions using the LOFAR 141 MHz and VLA 1.4 GHz 46″ resolution images.These regions are shown in the left panel of Fig. 10. The spectral steepening is more visible in the spectral index profile extracted across relic C. This result supports the classification of the source as a radio relic.

Other diffuse outskirts sources, D, F, and G (for labelling see Fig. 4), are more extended at 141 MHz compared to their sizes at 1.4 GHz. We refer to Table 3 for the measurements of their extension. Due to its elongated shape and location, source D was thought to be an internal filament (Brown et al. 2011). In our LOFAR image (e.g., in Fig. 10, left), the source further extends in the NW–SE direction and its north-western part is

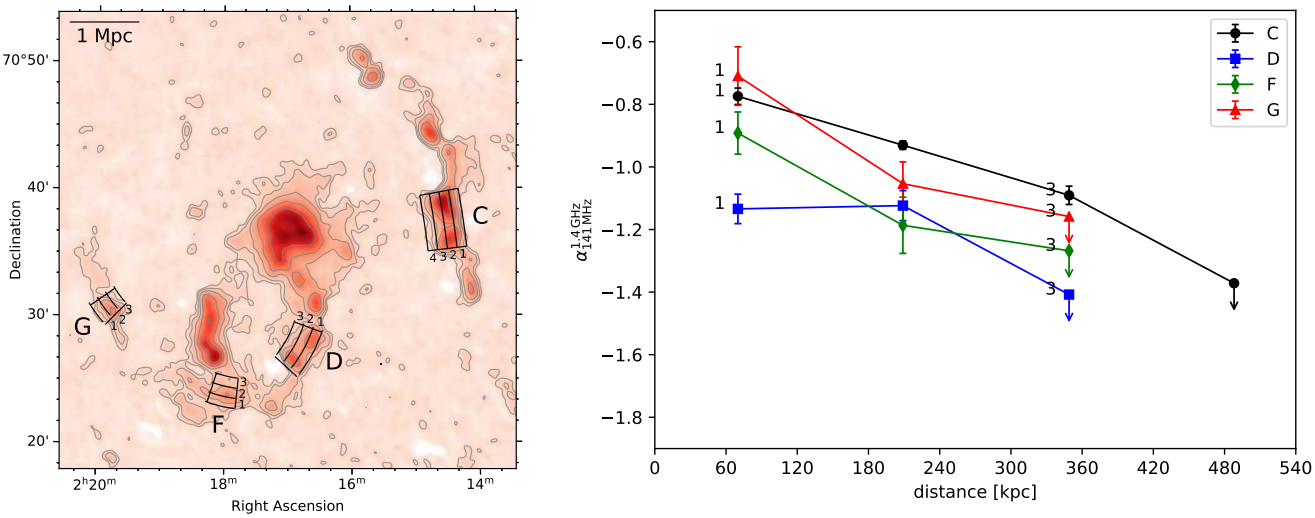

Fig. 10. *Left*: regions across the relics where spectral indices are extracted. The width of the regions is 46″, which is equal to the size of the synthesised beam. *Right*: spectral index profiles across the width of the relics in the left panel. The downward-pointing arrows indicate the upper limit of the spectral indices. The error bars show the 1σ uncertainties that are estimated from the image noise. The upper limits for the spectral indices (i.e. the arrows) are calculated using the upper limits of 2σ for the 1.4 GHz emission.

connected with the radio halo while its south-eastern region is connected with source F. The extension of source D along its width (i.e. 600 kpc in the NW–SE direction) suggests that it does not entirely consist of discrete sources.

As seen in Fig. 3, sources F and G are oriented in the east-west and north-south directions, respectively. On the basis of VLA 1.4 GHz images, Brown et al. (2011) identified both of these sources as radio relics. In the LOFAR image, source D is connected with source F. The clear connection between D and F suggests that they belong to a single structure with a projected size of 3.5 Mpc. If source G is also included, this increases to 5.1 Mpc. On the outer region of source F towards the south-east, an excess of diffuse emission, namely F1, is detected only at 141 MHz. We find that the spectral index of F1 is steeper than −1.7. The flux densities and spectral indices for these sources are reported in Table 3. The spectral index map presented in Fig. 6 reveals a hint of the spectral steepening across sources D, F, and G that is also seen in the spectral index profiles in Fig. 10 (right). The spectral indices across the relics are calculated in the similar manner as done for the source C (i.e. using the LOFAR 141 MHz and VLA 1.4 GHz 46″ resolution images and 46″-width regions). Based on the spectral and morphological properties of source D, we suggest that that it is a radio relic. Our results on the spectral steepening of F and G also support the relic classification of these sources by Brown et al. (2011).

Due to the low resolution of the VLA 1.4 GHz, sources B1+B2 (namely B in Brown et al. 2011) were classified as a single radio relic by Brown et al. (2011), but in our high-resolution image in Fig. 1, it is composed of a bent-tail radio galaxy to the north (i.e. B1) and a radio galaxy with two lobes to the south (i.e. B2). These radio galaxies are also detected with the SDSS and Pan-STARRS optical surveys. The Pan-STARRS cutout image in the B1+B2 region is shown in Appendix D. The SDSS identification is J021558.09+705040.1 ($z = 0.1962 \pm 0.0802$) and J021542.94+704832.3 for the northern and southern sources, respectively.

Source E1+E2 was unresolved in the VLA 1.4 GHz image and was identified as a single internal filament, namely E, by Brown et al. (2011). In our high-resolution LOFAR 141 MHz and VLA 1.5 GHz images shown in Figs. 1 and 2 (left), the source is resolved showing two parts (namely, E1 and E2). The southern part (E1) has a morphology typical of a double-lobe radio galaxy that has an SDSS optical counterpart (namely, J021814.33+702724.0 at RA = $02^{h}18^{m}14.33^{s}$, Dec = $+70^{d}27^{m}24.07^{s}$) reported in the SDSS catalogue (Alam et al. 2015). In Appendix D, the cutout Pan-STARRS colour image overlaid with the LOFAR contours shows better the optical counterpart for E1 (with object identification: 192540345597208886; Flewelling et al. 2020). No redshift information is available for this optical source in the SDSS and Pan-STARRS catalogues. The morphology of the lobes suggests that it could be a typical Fanaroff-Riley Class I (FR-I) galaxy. The southern lobe of the active galactic nucleus (AGN) is bent towards the east. The northern part (E2) has an elongated shape that connects with a lobe of the southern radio galaxy. We interpret the source E being a radio galaxy that is moving in the NW–SE direction and leaving the tail of radio emission behind.

4. Discussions

4.1. Radio halo

The presence of the radio halo in ClG0217 is confirmed with the LOFAR 141 MHz and VLA 1.5 GHz observations. The projected diameter of the halo at 141 MHz is 1.8 Mpc, which is more extended than previously detected at 1.4 GHz (Brown et al. 2011). The integrated spectral index for the halo between 141 MHz and 1.4 GHz is -1.02 ± 0.05. We discuss the spectral index properties and the correlation between thermal and non-thermal components below.

4.1.1. Spectral index variations

Spatial distribution of the spectral index in halos provides insight into the physical mechanisms responsible for the particle acceleration and magnetic field amplification in radio halos. In general, the spatial distribution of the spectral index provides information on turbulent scales, transport of particles and the magnetic field in the ICM. For example, homogeneous models where turbulence and magnetic field strength are uniform in

the emitting volume predict a uniform distribution of the spectral index. On the other hand, models with inhomogeneous turbulence and magnetic fields predict variations in the spectral indices in the entire emitting volume. The variations depend on how fast transport of particles, diffusion of magnetic field, and turbulent scales are.

Observations of radio halos have shown conflicting radial distributions of the spectral index. A few cases have been found where the average radial spectral index steepens in the peripheral regions (i.e. Abell 2744; Pearce et al. 2017, MACS J0717.5+3745; Rajpurohit et al. 2021a). In some other cases, no firm detection of radial spectral steepening feature is detected (e.g., Coma C[9]; Giovannini et al. 1993, Abell 665[9], Abell 2163[9]; Feretti et al. 2004, Abell 2219; Orrù et al. 2007). In some ongoing merging clusters, a uniform distribution of the spectral index over a large fraction of the halos was also detected (e.g., the Toothbrush cluster; van Weeren et al. 2016a; Rajpurohit et al. 2018; de Gasperin et al. 2020; Rajpurohit et al. 2020, the Sausage cluster; Hoang et al. 2017; Di Gennaro et al. 2018, and Abell 520; Hoang et al. 2019a).

In ClG0217, a spectral steepening is detected beyond 830 kpc from the cluster centre, as shown in Fig. 7 (right). However, within 680 kpc, the radial profile is roughly constant although there is a hint of radial spectral flattening. We note that X-ray SB discontinuities are detected at the edges of the northern and southern regions (within ~600 kpc; Zhang et al. 2020). Although the nature of the X-ray discontinuities (i.e. shock or cold front) is still unknown, they might affect the observed radio spectrum of the halo through the (re-)acceleration of the CRs and/or amplification of magnetic field. In some clusters, shock fronts are observed at the edges of radio halos, including Abell 520 (Markevitch et al. 2005), the Bullet cluster (Shimwell et al. 2014), the Coma cluster (i.e. the western edges of the halo; Brown & Rudnick 2011), and the Toothbrush (i.e. the southern edge; van Weeren et al. 2016a). Among these cases spectral flattening at the edges has been seen in two clusters, including the south-western region of Abell 520 (Hoang et al. 2019a) and the southern shock of the Toothbrush (Rajpurohit et al. 2018). The halo in ClG0217 might be the third case if future deep radio observations confirm the radial spectral trend.

4.1.2. Thermal and non-thermal correlation

The radio and X-ray emission in the halo of ClG0217 are found to be spatially correlated. In particular, as shown in Fig. 3, the radio and X-ray sub-structures in the central region of the halo are found to have similar shapes and orientations. Quantitatively, the radio and X-ray SB is consistent with the linear relation at 141 MHz with a correlation slope of $b_{141\,\mathrm{MHz}} = 1.03 \pm 0.09$. This slope is found to be sub-linear at 1.4 GHz with $b_{1.4\,\mathrm{GHz}} = 0.81 \pm 0.06$. The spatial correlation suggests a tight connection between the thermal gas and non-thermal components (i.e. relativistic electrons and magnetic field) in the ICM. Our results are similar to some cases where the radio and X-ray relation is linear/sub-linear (i.e. $b \sim 0.64 - 1$) regardless of the morphology of the radio halos (e.g., Feretti et al. 2001; Govoni et al. 2001a,b; Bruno et al. 2021; Rajpurohit et al. 2021a; Botteon et al. 2020b). Also, a lower value of b at a higher frequency suggests additional non-thermal processes in the outer regions of the halo where X-ray emission is fainter.

In the halo of ClG0217, the sub-linear slope at high frequencies could be related to the presence of X-ray SB discontinuities at the edges of the halo that might lead to a flattening of the spectrum (e.g., via adiabatic compression) and thus generate more flux in the periphery at 1.4 GHz. The hint of this trend (i.e. lower b at higher frequencies) is also seen in Abell 520, which hosts two X-ray SB jumps (i.e. a strong bow shock and a tentative shock/cool front) at the halo edges in Hoang et al. (2019b). They found $b_{145\,\mathrm{MHz}} = 0.34 \pm 0.11$, $b_{323\,\mathrm{MHz}} = 0.27 \pm 0.10$, and $b_{1.5\,\mathrm{GHz}} = 0.25 \pm 0.09$. However, an opposite trend (i.e. $b_{141\,\mathrm{MHz}} = 0.67 \pm 0.05$, $b_{1.5\,\mathrm{GHz}} = 0.81 \pm 0.09$, and $b_{3\,\mathrm{GHz}} = 0.98 \pm 0.09$) is also observed in the halo of MACS J0717.5+3745 in Rajpurohit et al. (2021a). The difference is likely due to the difference in the physical conditions in the two halos.

The simplest approach to turbulent re-acceleration models is to assume homogeneous conditions in the ICM. In this case, a broad spatial distribution of relativistic seed electrons and of the turbulence are assumed to be uniformed over a megaparsec-cubed volume. The synchrotron power is

$$P \propto \rho \frac{\delta V^3}{L} \frac{B^2}{B^2 + B_{\mathrm{CMB}}^2}, \tag{4}$$

where ρ is is the thermal particle density, δV is the turbulent velocity, and L is the corresponding turbulent scale (e.g., Brunetti & Vazza 2020). In the dynamo conditions, $B^2 \propto \rho d V^2$, and for $B < B_{\mathrm{CMB}} = 3.2 \times (1+z)^2$ μG the synchrotron power scales with $P \propto \rho^2$ implying a linear radio–X-ray correlation (Beresnyak 2012; Brunetti & Vazza 2020). As a consequence, the linear correlation that is observed at 141 MHz between X-ray and synchrotron SB would imply a magnetic field smaller than 4.5 μG in the halo volume; stronger fields would indeed generate a sub-linear scaling correlation. In this case, the sub-linear coefficient that is measured at 1.4 GHz may imply that additional mechanisms (e.g., compression at the edges of the halo) contribute to the re-acceleration of particles in the outer regions of the halo (i.e. low X-ray SB regions). This would also be consistent with the hint of a radial spectral flattening discussed in Sect. 3.1.2.

4.2. Radio relics

4.2.1. Shock Mach numbers

The elongated shape, location, and the lack of optical counterparts of C, D, F, and G suggest that they are radio relics. The spectral steepening across their width shown in Fig. 10 further supports the classification. In the context of direct shock acceleration model, the relativistic electrons emitting the radio synchrotron emission in radio relics are accelerated directly from thermal pool at shock fronts. The energy distribution of these relativistic electrons follows the standard power-law function $\mathrm{d}N(p)/\mathrm{d}p \propto p^{-\delta_{\mathrm{inj}}}$, where $\mathrm{d}N(p)$ is the number of particles in the energy range between p and $p + \mathrm{d}p$, and $\delta_{\mathrm{inj}} = 1 - 2\alpha_{\mathrm{inj}}$ is the energy index. The spectral index of the injected relativistic electrons, α_{inj}, non-linearly depends on the Mach number of the shocks (e.g., Blandford & Eichler 1987),

$$\mathscr{M} = \sqrt{\frac{2\alpha_{\mathrm{inj}} - 3}{2\alpha_{\mathrm{inj}} + 1}}, \tag{5}$$

where $\alpha_{\mathrm{inj}} > -0.5$. After being injected from the shock fronts, the relativistic electrons start to lose their energy in the

[9] The uncertainty of the spectral measurement in these cases is high due to the mismatching of the *uv* coverages in the observations, as pointed out by Botteon et al. (2020b).

Table 5. Shock Mach numbers for radio relics.

Source	$\alpha_{\rm inj}$	$\mathscr{M}_{\rm inj}$	$\alpha_{\rm int}$	$\mathscr{M}_{\rm int}$
C	-0.72 ± 0.05	$3.2^{+0.4}_{-0.3}$	-1.01 ± 0.05	14
D	-1.14 ± 0.07	$2.0^{+0.1}_{-0.1}$	-1.34 ± 0.06	$2.6^{+0.2}_{-0.2}$
F	-0.93 ± 0.08	$2.4^{+0.2}_{-0.2}$	-1.09 ± 0.06	$4.8^{+3.4}_{-1.0}$
G	-0.97 ± 0.16	$2.3^{+0.4}_{-0.2}$	-1.00 ± 0.06	$\gtrsim 5.8$

downstream region due to the synchrotron and inverse-Compton radiation, resulting in a steeper integrated spectral index over the source volume (Ginzburg & Syrovatskii 1969),

$$\alpha_{\rm int} = \alpha_{\rm inj} - 0.5. \quad (6)$$

The Mach numbers can be estimated through the discontinuity of X-ray SB or temperature jumps that associate with the particle density across the shock fronts. However, the X-ray *Chandra* data we use in this study are too shallow or do not cover the regions of the radio relics, which does not allow us to search for the shocks at these regions with the X-ray data. To estimate the strength of the shocks associated with the relics, we calculate their Mach numbers using the injected spectra that are measured in the injection regions and the volume of the sources. In both methods, we use the LOFAR 141 MHz and VLA 1.4 GHz 46″ resolution images (see Table 2 for image properties). We measure the injection spectral indices in the outer regions of relics C, D, F, and G that have flattest spectra where the relativistic electrons are injected. Taking into account the image resolution, we set the width of the extracted regions to be the same as the beam size (i.e. 46″). The corresponding Mach numbers are estimated using Eq. (5) and given in Table 5. The Mach numbers for these relics range between 2.0 and 3.2 that are typically found for shocks in merging clusters of galaxies (e.g., Markevitch & Vikhlinin 2007).

Alternatively, the Mach numbers can be calculated from the volume integrated spectral index via Eqs. (5) and (6). We use the integrated spectral indices for the relics in Table 3. The resulting Mach numbers for D and F are $\mathscr{M}_{\rm D}^{\rm int} = 2.6^{+0.2}_{-0.2}$ and $\mathscr{M}_{\rm F}^{\rm int} = 4.8^{+3.4}_{-1.0}$, respectively. These estimates are higher than those we estimated with the injection spectral indices, as summarised in Table 5. Previous studies have also found this systematic offsets between the estimates that use spatially resolved maps and integrated spectra (e.g., Stroe et al. 2013; Hoang et al. 2017, 2018). However, the integrated spectral index method when used for relics C and G results in unrealistic Mach numbers for merger shocks. For instance, the integrated spectral index for C is -1.01 ± 0.06; this corresponds to a shock Mach number of $\mathscr{M}_{\rm C}^{\rm int} = 14$, which cannot be found in merging galaxy clusters as it requires a very different particle acceleration efficiency than those in the other relics, D and F. For relic G, the integrated spectral index of -1.00 ± 0.06 implies an injection spectral index of -0.50 ± 0.06, which cannot be used for Eq. (6) (i.e. the square root of a real negative number). This implies that relic G is a clear example where Eq. (6) is invalid. In other words, the cooling time of the radio-emitting particles is longer than crossing time of the shock. In case of the lowest 1σ limit on the integrated spectral index (i.e. $\alpha = -1.06$), the lower limit for the Mach number is $\mathscr{M}_{\rm G}^{\rm int} \gtrsim 5.8$.

Estimating the Mach numbers through spectral index maps or estimating them through integrated spectral indices both have pros and cons, as discussed in Sect. 4.1.3 of Hoang et al. (2017). In the former method, the injection index is mostly affected by the projection effect, beside the spatial resolution and the misalignment of radio images. The measurement bias for the injection index is reduced when the shock propagates on the plane of the sky as it minimises the mixture of relativistic electrons with different spectra in the downstream region. Although the plane of shock waves in ClG0217 is unconstrained, it is unlikely to deviate significantly from the plane of the sky as it is typically found for double-relic clusters. Hence, the injection spectral indices obtained directly from the spectral index map is likely to provide more reliable estimates of the shock Mach numbers associated with the relics. However, we still need further investigation with optical observations to constrain on the merger dynamics of the cluster.

Moreover, the orientation of the major axes of relics D, F, and G suggests that they are related to a structure, which is supported by the Mach numbers of these relics not being largely different (i.e. 2.0 – 2.4; Table 5). When using the integrated spectral index, we are not biased by the spatial resolution, the projection effect, or the misalignment of the radio images. However, we assume that radio relics are caused by planar shock waves (i.e. Eq. (6)). Simulations by Kang (2015a,b) found that this assumption does not hold for spherical shocks that are typically found in merging systems (due to their arc-like shape). The deviation significantly increases in time as the shock propagates towards the outskirts. This explanation is in line with the fact that the radial distance increases from 1.6 Mpc to 2.5 Mpc and 2.9 Mpc for D, F, and G, respectively. As a result, the Mach numbers inferred from the integrated spectral indices largely differ from those using the spectral index map (i.e. $\mathscr{M}_{\rm D}^{\rm int} = 2.6^{+0.2}_{-0.2}$ and $\mathscr{M}_{\rm F}^{\rm int} = 4.8^{+3.4}_{-1.0}$, but it is unusable for the extreme case of relic G). On the other hand, the Mach number discrepancy for C is more significant than that of F although relic C is closer to the cluster centre than F. This could imply that the shocks in the west (for C) and southeast (for F) directions travels through different physical environments (Domínguez-Fernández et al. 2020). In Fig. 11 we show the Mach number obtained from integrated and injection index as a function of distance of these relics from the cluster centre. The discrepancy for the shock Mach numbers associated with the relics are clearly visible.

4.2.2. Particle acceleration efficiency

For relics associated with $\mathscr{M} \gtrsim 2.5$ shocks, a direct acceleration of thermal electrons via DSA might be possible as it requires a lower acceleration efficiency ($\xi \lesssim 0.1$, Botteon et al. 2020a; Brunetti & Jones 2014). We explore the possibility of direct shock acceleration for relic C that is related to the strongest ($\mathscr{M}_{\rm C}^{\rm inj} = 3.2^{+0.4}_{-0.3}$) shock in the cluster. In Fig. 12 we present the acceleration efficiency as a function of downstream magnetic field strength for relic C with different Mach numbers, ranging between 2.5 and 5. The relation between the radio power of the relic, the efficiency, the Mach numbers, and other properties of the downstream medium is based on Eq. (32) of Hoeft & Bruggen (2007), taking a recent revision of the relation into account (for the updated expression, see Rajpurohit et al. 2021b). In the calculation of the acceleration efficiency, we use an average temperature of 5 keV at the relic location (i.e. also R_{200}) that is estimated using a typical temperature profile for clusters (Pratt et al. 2007) and a cluster average temperature of 8.3 keV (Zhang et al. 2020). The downstream electron density is estimated to be 2.6×10^{-5} cm^{-3}, based on a typical gas density at the cluster virial radius. The shock surface area is assumed to be the area of a spherical cone with an area of 4 Mpc^2. The radio power at 1.4 GHz is taken from the measurement of the

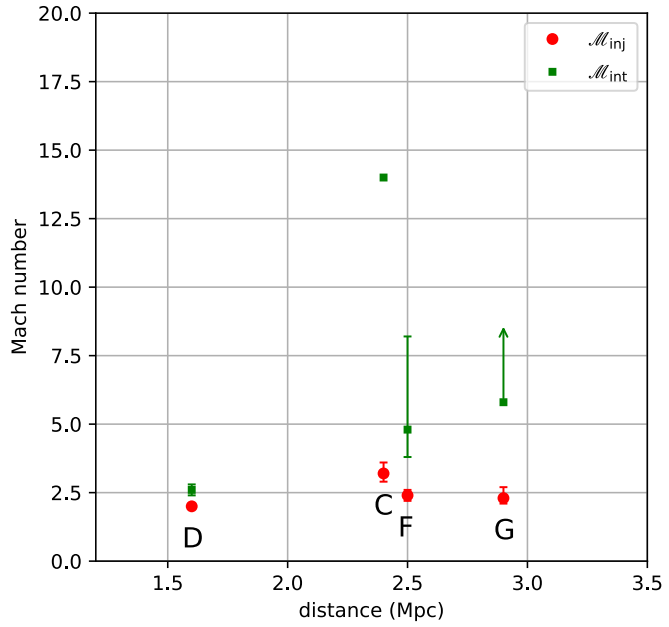

Fig. 11. Scatter plot of the shock Mach numbers and the distance of the relics from the cluster centre.

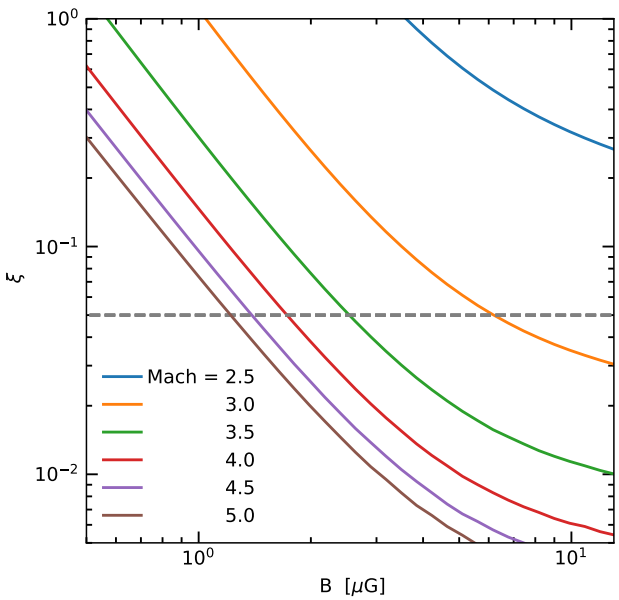

Fig. 12. Particle acceleration efficiency, ξ, as a function of the downstream magnetic field strength, B, for relic C with different Mach numbers. The horizontal dashed line indicates an efficiency of 5 percent.

VLA 1.4 GHz (i.e. $P_{1.4\,\rm GHz} = 1.85 \times 10^{24}\,\rm W\,Hz^{-1}$). With these parameters fixed the shock acceleration efficiency can be given as a function of downstream magnetic field and Mach number.

Figure 12 shows that the acceleration efficiency required to produce the relic brightness decreases when the downstream magnetic field and the shock Mach number increase. For instance, the efficiency needs to be less than 5 percent for Mach numbers of $\mathscr{M} \gtrsim 3.5$ in the $B \gtrsim 3\,\mu$G field. In these cases, a direct acceleration of thermal electrons might be still possible for relic C, although it depends on our assumptions regarding, for example, the geometry of the shocks, the temperature profile of the cluster, and the typical gas density at the virial radius, which we are unable to confirm with the present data. Nevertheless, a pre-existing population of mildly relativistic electrons prior to the re-acceleration of the shock will provide an additional source of energy for the relic lowering the required acceleration efficiency of the shock.

4.2.3. Shock re-acceleration of fossil electrons

Current theoretical models predict a smaller efficiency (i.e. a few percent) for low-Mach-number ($\mathscr{M} \lesssim 2.5$) shocks (e.g., Kang & Jones 2005; Kang & Ryu 2013). A possibility for the generation of the relics by these shocks is that the radio-emitting relativistic electrons are re-accelerated from a population of mildly relativistic electrons from, for example, previous cluster mergers, AGN activities, or supernovae (e.g., van Weeren et al. 2013; Bonafede et al. 2014; Shimwell et al. 2015; Botteon et al. 2016; van Weeren et al. 2017). In this re-acceleration scenario, the energy that is required to be transferred to the radio-emitting relativistic electrons decreases. Hence, the acceleration efficiency required to produce the brightness of the relics is lower. In addition, unlike the thermal population that smoothly distributes over the cluster volume, fossil plasma from, for example, AGN activities typically has small-scale structure that is similar to that of the relics (e.g., Bonafede et al. 2014).

In ClG0217, the relics, excluding C, are associated with low-Mach-number ($\mathscr{M} = 2.0$–2.4) shocks that are likely to be too weak for a direct acceleration of the thermal electrons and, as discussed, requires the presence of fossil plasma ahead of the shock. Supporting evidence for this scenario in ClG0217 is that the relics show a clumpy structure and extended radio emission in front of the shock fronts. Our result is in line with Brown et al. (2011) where the re-acceleration of fossil electrons by AGN activities was pointed out to explain the variations in the radio SB of the relics (C, F, and G). In addition, the location of C1 and F1 in the LOFAR maps suggests a possible connection with relics C and F. Furthermore, the steep ($\alpha < -1.7$) spectral properties of C1 and F1 support their nature being fossil plasma, rather than being caused by merger shocks. However, the present LOFAR observations do not detect diffuse faint emission in front of the entire length of the relics (C and F), suggesting that the radio emission of the fossil electrons in these regions is faint; this requires deeper observations to confirm.

4.3. Spectral variations over source E

To examine the spectral index in source E, we extract 141 MHz–1.5 GHz spectra in the square regions from the centre of the southern part towards the north. These regions are shown in the left panel of Fig. 13. The size of each region is equal to the beam size of the high-resolution spectral index (i.e. $16'' \times 16''$, corresponding a physical size of 49 kpc × 49 kpc). The projected distance along these 18 regions is 870 kpc. In the middle panel of Fig. 13, we present the extracted spectra. The spectral index steepens from the central region of the AGN towards the northern lobe (i.e. from -0.82 ± 0.08 in region 1 to -1.10 ± 0.15 in region 5). In the regions between the southern and northern parts of E (regions 6–8), the diffuse emission is undetected at 1.5 GHz, implying a steep spectral index below -1.25. The spectral steepening feature is typically observed in lobes of AGN, which is due to the energy losses via synchrotron and inverse-Compton radiation. Farther to the north, the spectral index becomes flat. The index increases up to -0.68 ± 0.11 in the northern regions (i.e. regions 13–15) where the source is significantly brighter at 1.5 GHz.

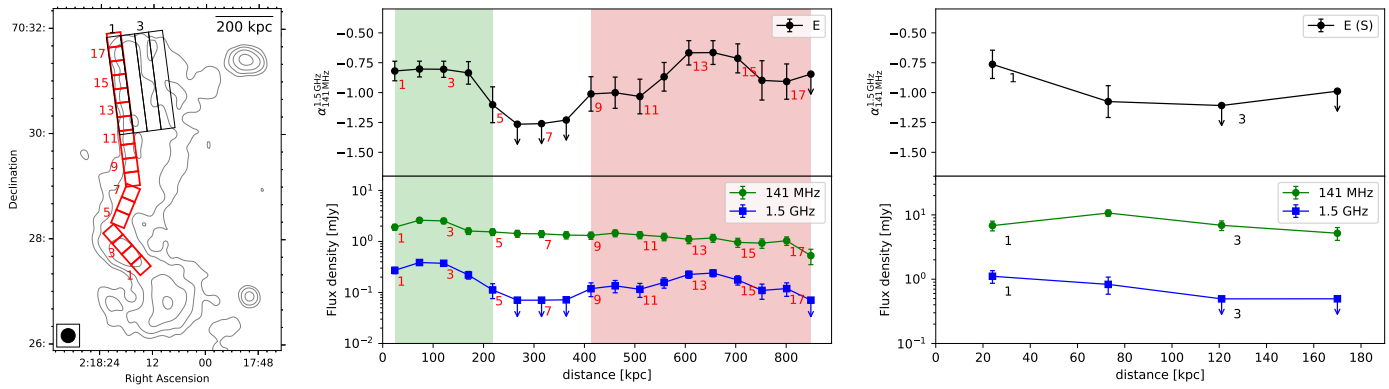

Fig. 13. *Left*: regions over source E (i.e. E1+E2); SB and spectral indices have been extracted and are shown in the middle and right panels. *Middle*: SB and spectral index profiles along the S–N direction (i.e. red boxes). *Right*: similar to the middle panel, but with the profiles calculated in the E–W direction (i.e. black rectangles).

The spectral flattening in the northern part of source E (i.e. E2) suggests the presence of a physical process that re-accelerates the fossil plasma of the southern AGN and/or amplifies the magnetic field in the regions. A possible origin of such a process is a merger shock that is propagating eastwards. One such example has been observed in the merging galaxy cluster Abell 3411-3412 (van Weeren et al. 2017). In this case, fossil electrons from an AGN lobe lose their energy by spectral ageing before they are re-accelerated or adiabatically compressed by a merger shock. The re-acceleration leads to the spectral flattening of the radio emission in the region of the shock front. An additional feature of the shock re-acceleration is that the spectral index also steepens in the direction behind the shock front or towards the cluster centre as for outward moving shocks. Some other examples for the relic-AGN connection and/or interaction between AGN in shocks include the southern relic of the Sausage (Di Gennaro et al. 2018), Abell 781 (Botteon et al. 2019), the eastern relic of RXC J1314.4–2515 (Stuardi et al. 2019), the north-eastern relic in PLCK G287.0+32.9 (Bonafede et al. 2014), and the southern relic of PSZ2 G096.88+24.18 (Jones et al. 2021).

To examine the possible spectral ageing behind the northern part of E, we extract spectra in the regions across the width of its northern part (i.e. in east-west direction). These regions are shown in black in the left panel of Fig. 13. The width of each region is equal to the resolution of the LOFAR 141 MHz and VLA 1.5 GHz images (i.e. 16″). The corresponding spectral index profile is shown in the right panel of Fig. 13, suggesting a spectral steepening from east to west (i.e. from -0.76 ± 0.12 to -1.08 ± 0.13). This spectral steepening further supports our speculation that the northern part of source E is re-accelerated or compressed by an outward moving shock. Using Eq. (5) and the spectral index of -0.76 ± 0.12 in the eastern region of the northern part of E, we find that the Mach number of the possible shock is $\mathscr{M}_{\rm E} = 2.9^{+1.0}_{-0.4}$. In this case, we use the integrated spectral index for the northern part (i.e. -1.20 ± 0.05); the corresponding Mach number is $\mathscr{M}_{\rm E}^{\rm int} = 3.3^{+0.5}_{-0.3}$, which is consistent within 1σ with the estimate directly using the spectral index map. Although the uncertainties of the Mach numbers are high, the consistency between the Mach numbers for the northern part of E might be due to the fact that the source E is closer to the cluster centre (e.g., compared with C, F, and G) where the approximation in Eq. (6) still holds. The presence of the shock front, if it exists, can be confirmed by future X-ray observations that we are unable to check with the current data.

5. Conclusions

In this paper we present LOFAR 141 MHz and VLA 1.5 GHz observations of the merging galaxy cluster ClG0217, which was previously studied with the VLA at 325 MHz and 1.4 GHz by Brown et al. (2011). The LOFAR observations provide the first radio images of the cluster at frequencies below 325 MHz and confirm the presence of a giant radio halo and multiple radio relics in the cluster. To study the nature of these diffuse sources, we made spectral index maps of the cluster using the LOFAR and VLA datasets. We also made use of the archival *Chandra* data to investigate the correlation between the thermal and non-thermal emission from the central radio halo and to search for discontinuities in the X-ray SB. We summarise the results below:

1. The radio halo with a projected size of 1.8 Mpc is observed to be more extended at 141 MHz than at the higher frequency of 1.4 GHz. Its flux density at 141 MHz is 623.6 ± 62.7 mJy, corresponding to a radio power of $P_{141\,\rm MHz} = (56.9 \pm 5.7) \times 10^{24}$ W Hz^{-1}. The radio power of ClG0217 is roughly in line with the prediction from the radio power–mass relation.
2. The integrated spectrum of the radio halo in ClG0217 is -0.78 ± 0.16 between 141 MHz and 325 MHz and steepens to -1.16 ± 0.07 between 325 MHz and 1.4 GHz. This suggests the radio halo has a curved spectrum. However, further observations are needed to confirm this due to the low resolution of the 325 MHz data, which may lead to an imperfect subtraction of compact sources that are contaminating the halo flux measurement.
3. The non-thermal radio and thermal X-ray emission in the halo region where the radio and X-ray emission is detected above 2σ are positively correlated. At 141 MHz, the correlation is consistent with a linear relation, $\log_{10} I_R \propto b \times \log_{10} I_X$, where $b_{\,141\,\rm MHz} = 1.03 \pm 0.09$. However, at 1.4 GHz the correlation follows a sub-linear relation with $b_{1.4\,\rm GHz} = 0.81 \pm 0.06$. The results suggest that the non-thermal components at high frequencies (1.4 GHz) decline more slowly than those at low frequencies (141 MHz). This implies that there are additional mechanisms (i.e. particle acceleration and/or magnetic field amplification via shocks or cold fronts) or inhomogeneous conditions (e.g., stronger turbulence) in the outer regions of the halo relative to what is found in the X-ray data. However, our high spectral index uncertainties do not allow us to draw a firm conclusion on this as we find that the spectral index is roughly constant within a radius of 680 kpc.
4. At 141 MHz, relics D and F are connected and likely belong to the same source, with a projected size of 3.5 Mpc, which

makes this structure the largest radio relic found to date. Source G is possibly part of this structure and, if included, could increase the relic size to 5.1 Mpc; however, deeper observations are needed to confirm this.

5. The spectral steepening is found across the width of relics C, D, F, and G, implying the spectral ageing of the sources. Using the spectral indices at the outer edges of the relics, we find that the relics are generated by low-Mach-number shocks that are unlikely to directly accelerate thermal electrons to create the observed SB in the relics. An extra source of energy with steep spectra (e.g., from fossil electrons) is required. The presence of such steep-spectrum sources (i.e. C1 and F1) in our LOFAR data supports this re-acceleration scenario.
6. Thanks to the high-resolution images from the LOFAR 141 MHz and VLA 1.5 GHz observations, source E is resolved into a double-lobe radio galaxy in the south and an elongated tail in the north (i.e. E1 and E2). We find that the spectral index in the region between E1 and E2 flattens, suggesting a possible re-acceleration by a merger shock that is moving outwards in the northern region of E. The spectral steepening in the east-west direction further supports this scenario.

The late-stage merging galaxy cluster ClG0217 is a dynamically rich system that hosts multiple radio relics and a giant radio halo. These extended radio sources are ideal locations for studying particle (re-)acceleration, turbulence, and magnetic field amplification in the late stage of a cluster merger. Our study, using multi-wavelength datasets, provides new insights into the nature of the sources (i.e. classification, morphology, spectral properties, and interplay between thermal and non-thermal components). However, due to the quality of the current data, we are unable to confirm some aspects associated with, for example, radio spectral emission at the X-ray discontinuities in the halo, spectral flattening in the north of source E, and the presence of shock fronts at the location of the relics. Further work using multi-wavelength (radio, X-ray, optical) observations will be necessary to further investigate these aspects.

Acknowledgements. D.N.H. and A.B. acknowledge support from the ERC through the grant ERC-Stg DRANOEL n. 714245. MB acknowledges support from the Deutsche Forschungsgemeinschaft under Germany's Excellence Strategy – EXC 2121 "Quantum Universe" – 390833306. X.Z. acknowledges support from China Scholarship Council. SRON is supported financially by NWO, The Netherlands Organization for Scientific Research. R.J.v.W. acknowledges support from the ERC Starting Grant ClusterWeb 804208. A.B. acknowledges support from the VIDI research programme with project number 639.042.729, which is financed by the Netherlands Organisation for Scientific Research (NWO). AS is supported by the Women In Science Excel (WISE) programme of the Netherlands Organisation for Scientific Research (NWO), and acknowledges the World Premier Research Center Initiative (WPI) and the Kavli IPMU for the continued hospitality. SRON Netherlands Institute for Space Research is supported financially by NWO. GB acknowledges partial support from INAF mainstream program "Galaxy clusters science with LOFAR" LOFAR (van Haarlem et al. 2013) is the Low Frequency Array designed and constructed by ASTRON. It has observing, data processing, and data storage facilities in several countries, which are owned by various parties (each with their own funding sources), and that are collectively operated by the ILT foundation under a joint scientific policy. The ILT resources have benefited from the following recent major funding sources: CNRS-INSU, Observatoire de Paris and Université d'Orléans, France; BMBF, MIWF-NRW, MPG, Germany; Science Foundation Ireland (SFI), Department of Business, Enterprise and Innovation (DBEI), Ireland; NWO, The Netherlands; The Science and Technology Facilities Council, UK; Ministry of Science and Higher Education, Poland; The Istituto Nazionale di Astrofisica (INAF), Italy. This research made use of the Dutch national e-infrastructure with support of the SURF Cooperative (e-infra 180169) and the LOFAR e-infra group. The Jülich LOFAR Long Term Archive and the German LOFAR network are both coordinated and operated by the Jülich Supercomputing Centre (JSC), and computing resources on the supercomputer JUWELS at JSC were provided by the Gauss Centre for Supercomputing e.V. (grant CHTB00) through the John von Neumann Institute for Computing (NIC). This research made use of the University of Hertfordshire high-performance computing facility and the LOFAR-UK computing facility located at the University of Hertfordshire and supported by STFC [ST/P000096/1], and of the Italian LOFAR IT computing infrastructure supported and operated by INAF, and by the Physics Department of Turin university (under an agreement with Consorzio Interuniversitario per la Fisica Spaziale) at the C3S Supercomputing Centre, Italy. The scientific results reported in this article are based on data obtained from the *Chandra* Data Archive. This research has made use of software provided by the *Chandra* X-ray Center (CXC) in the application packages CIAO, ChIPS, and Sherpa. The National Radio Astronomy Observatory is a facility of the National Science Foundation operated under cooperative agreement by Associated Universities, Inc.

References

Alam, S., Albareti, F. D., Prieto, C. A., et al. 2015, ApJS, 219
Arnaud, M., Pointecouteau, E., & Pratt, G. W. 2007, A&A, 474, L37
Bell, A. R. 1978, MNRAS, 182, 147
Beresnyak, A. 2012, Phys. Rev. Lett., 108, 035002
Blandford, R., & Eichler, D. 1987, Phys. Rep., 154, 1
Bonafede, A., Intema, H. T., Brüggen, M., et al. 2014, ApJ, 785, 1
Botteon, A., Gastaldello, F., Brunetti, G., & Dallacasa, D. 2016, MNRAS, 460, L84
Botteon, A., Shimwell, T. W., Bonafede, A., et al. 2019, A&A, 622, A19
Botteon, A., Brunetti, G., Ryu, D., & Roh, S. 2020a, A&A, 634, A64
Botteon, A., Brunetti, G., van Weeren, R. J., et al. 2020b, ApJ, 897, 93
Boxelaar, J., van Weeren, R., & Botteon, A. 2021, Astron. Comput., 35, 100464
Brown, S., & Rudnick, L. 2011, MNRAS, 412, 2
Brown, S., Duesterhoeft, J., & Rudnick, L. 2011, ApJ, 727, L25
Brunetti, G., & Lazarian, A. 2007, MNRAS, 378, 245
Brunetti, G., & Lazarian, A. 2011, MNRAS, 410, 127
Brunetti, G., & Jones, T. W. 2014, Int. J. Mod. Phys. D, 23, 1430007
Brunetti, G., & Lazarian, A. 2016, MNRAS, 458, 2584
Brunetti, G., & Vazza, F. 2020, Phys. Rev. Lett., 124, 051101a
Brunetti, G., Setti, G., Feretti, L., & Giovannini, G. 2001, MNRAS, 320, 365
Brunetti, G., Cassano, R., Dolag, K., & Setti, G. 2009, A&A, 507, 661
Bruno, L., Rajpurohit, K., Brunetti, G., et al. 2021, A&A, 650, A44
Cassano, R., Brunetti, G., & Setti, G. 2006, MNRAS, 369, 1577
de Gasperin, F., Dijkema, T. J., Drabent, A., et al. 2019, A&A, 622, A5
de Gasperin, F., Brunetti, G., Brüggen, M., et al. 2020, A&A, 642, A85
Delain, K. M., & Rudnick, L. 2006, Astron. Nachr., 327, 561
Di Gennaro, G., van Weeren, R. J., Hoeft, M., et al. 2018, ApJ, 865, 24
Domínguez-Fernández, P., Brüggen, M., Vazza, F., et al. 2020, MNRAS, 500, 795
Drury, L. O., & O'C Drury, L., 1983, Reports Prog. Phys., 46, 973
Enßlin, T. A., Biermann, P. L. P., Klein, U., et al. 1998, A&A, 409, 395
Feretti, L., Fusco-Femiano, R., Giovannini, G., & Govoni, F. 2001, A&A, 373, 106
Feretti, L., Orru, E., Brunetti, G., et al. 2004, A&A, 423, 111
Flewelling, H. A., Magnier, E. A., Chambers, K. C., et al. 2020, ApJS, 251, 7
Foreman-Mackey, D., Hogg, D. W., Lang, D., & Goodman, J. 2013, PASP, 125, 306
Ginzburg, V., & Syrovatskii, S. 1969, The Origin of Cosmic Rays (New York: Gordon and Breach)
Giovannini, G., Feretti, L., Venturi, T., Kim, K.-T., & Kronberg, P. P. 1993, ApJ, 406, 399
Govoni, F., Enßlin, T. A., Feretti, L., & Giovannini, G. 2001a, A&A, 369, 441
Govoni, F., Feretti, L., Giovannini, G., et al. 2001b, A&A, 819, 803
Hoang, D. N., Shimwell, T. W., Stroe, A., et al. 2017, MNRAS, 471, 1107
Hoang, D. N., Shimwell, T. W., van Weeren, R. J., et al. 2018, MNRAS, 478, 2218
Hoang, D. N., Shimwell, T. W., van Weeren, R. J., et al. 2019a, A&A, 622, A20
Hoang, D. N., Shimwell, T. W., van Weeren, R. J., et al. 2019b, A&A, 622, A21
Hoeft, M., & Bruggen, M. 2007, MNRAS, 375, 77
Intema, H. T., Jagannathan, P., Mooley, K. P., & Frail, D. A. 2017, A&A, 598, A78
Jones, A., de Gasperin, F., Cuciti, V., et al. 2021, MNRAS, 505, 4762
Kang, H. 2015a, J. Korean Astron. Soc., 48, 9
Kang, H. 2015b, J. Korean Astron. Soc., 48, 155
Kang, H., & Jones, T. W. 2005, ApJ, 620, 44
Kang, H., & Ryu, D. 2011, ApJ, 734, 18
Kang, H., & Ryu, D. 2013, ApJ, 764, 95
Kang, H., Ryu, D., & Jones, T. W. 2012, ApJ, 756, 97
Kelly, B. C. 2007, ApJ, 665, 1489
Liang, H., Hunstead, R. W., Birkinshaw, M., & Andreani, P. 2000, ApJ, 544, 686

Markevitch, M., & Vikhlinin, A. 2007, Phys. Rep., 443, 1
Markevitch, M., Govoni, F., Brunetti, G., & Jerius, D. 2005, ApJ, 627, 733
McMullin, J., Waters, B., Schiebel, D., Young, W., & Golap, K. 2007, in Astron. Data Anal. Softw. Syst. XVI, eds. R. Shaw, F. Hill, & D. Bell, ASP Conf. Ser., 376, 127
Murgia, M., Govoni, F., Markevitch, M., et al. 2009, A&A, 499, 679
Offringa, R., & Smirnov, O. 2017, MNRAS, 16, 1
Offringa, A. R., McKinley, B., Hurley-Walker, N., et al. 2014, MNRAS, 444, 606
Orrù, E., Murgia, M., Feretti, L., et al. 2007, A&A, 467, 943
Owers, M. S., Nulsen, P. E., Couch, W. J., & Markevitch, M. 2009, ApJ, 704, 1349
Pearce, C. J. J., van Weeren, R. J., Andrade-Santos, F., et al. 2017, ApJ, 845, 81
Perley, R. A., & Butler, B. J. 2017, ApJS, 230, 7
Petrosian, V. 2001, ApJ, 557, 560
Pinzke, A., Oh, S. P., & Pfrommer, C. 2017, MNRAS, 465, 4800
Pratt, G. W., Böhringer, H., Croston, J. H., et al. 2007, A&A, 461, 71
Rajpurohit, K., Hoeft, M., van Weeren, R. J., et al. 2018, ApJ, 852, 65
Rajpurohit, K., Hoeft, M., Vazza, F., et al. 2020, A&A, 636, A30
Rajpurohit, K., Brunetti, G., Bonafede, A., et al. 2021a, A&A, 646, A135
Rajpurohit, K., Vazza, F., van Weeren, R. J., et al. 2021b, A&A, 654, A41
Rengelink, R. B., Tang, Y., de Bruyn, A. G., et al. 1997, A&AS, 124, 259
Roettiger, K., Burns, J. O., & Stone, J. M. 1999, ApJ, 518, 603
Rudnick, L., Delain, K. M., & Lemmerman, J. A. 2006, Astron. Nachr., 327, 549
Sarazin, C. L. C. C. L. 2002, Springer, 272, 1
Shimwell, T. W., Brown, S., Feain, I. J., et al. 2014, MNRAS, 440, 2901
Shimwell, T. W., Markevitch, M., Brown, S., et al. 2015, MNRAS, 449, 1486
Shimwell, T. W., Röttgering, H. J. A., Best, P. N., et al. 2017, A&A, 598, A104
Shimwell, T. W., Tasse, C., Hardcastle, M. J., et al. 2019, A&A, 622, A1
Stroe, A., van Weeren, R. J., Intema, H. T., et al. 2013, A&A, 555, A110
Stuardi, C., Bonafede, A., Wittor, D., et al. 2019, MNRAS, 489, 3905
Tasse, C., Shimwell, T., Hardcastle, M. J., et al. 2021, A&A, 648, A1
van Haarlem, M. P., Wise, M. W., Gunst, A. W., et al. 2013, A&A, 556, A2
van Weeren, R. J., Fogarty, K., Jones, C., et al. 2013, ApJ, 769, 101
van Weeren, R. J., Williams, W. L., Hardcastle, M. J., et al. 2016a, ApJS, 223, 2
van Weeren, R. J., Brunetti, G., Brüggen, M., et al. 2016b, ApJ, 818, 204
van Weeren, R. J., Andrade-Santos, F., Dawson, W. A., et al. 2017, Nat. Astron., 1, 5
van Weeren, R. J., de Gasperin, F., Akamatsu, H., et al. 2019, Space Sci. Rev., 215, 16
van Weeren, R. J., Shimwell, T. W., Botteon, A., et al. 2021, A&A, 651, A115
Vazza, F., & Brüggen, M. 2014, MNRAS, 437, 2291
Zhang, X., Simionescu, A., Kaastra, J. S., et al. 2020, A&A, 642, L3

Appendix A: High-resolution intensity images

The high-resolution intensity images of the cluster ClG0217 are shown in Fig. A.1. The images are obtained with LOFAR 141 MHz and VLA 1.4GHz data with a combination of *uv* cut of below 2 $k\lambda$ and `robust` weightings (i.e. −0.25 and −2 for the LOFAR and VLA data, respectively) to filter out the large-scale emission from the cluster. These images are used to make models of compact sources, which are then subtracted from the data.

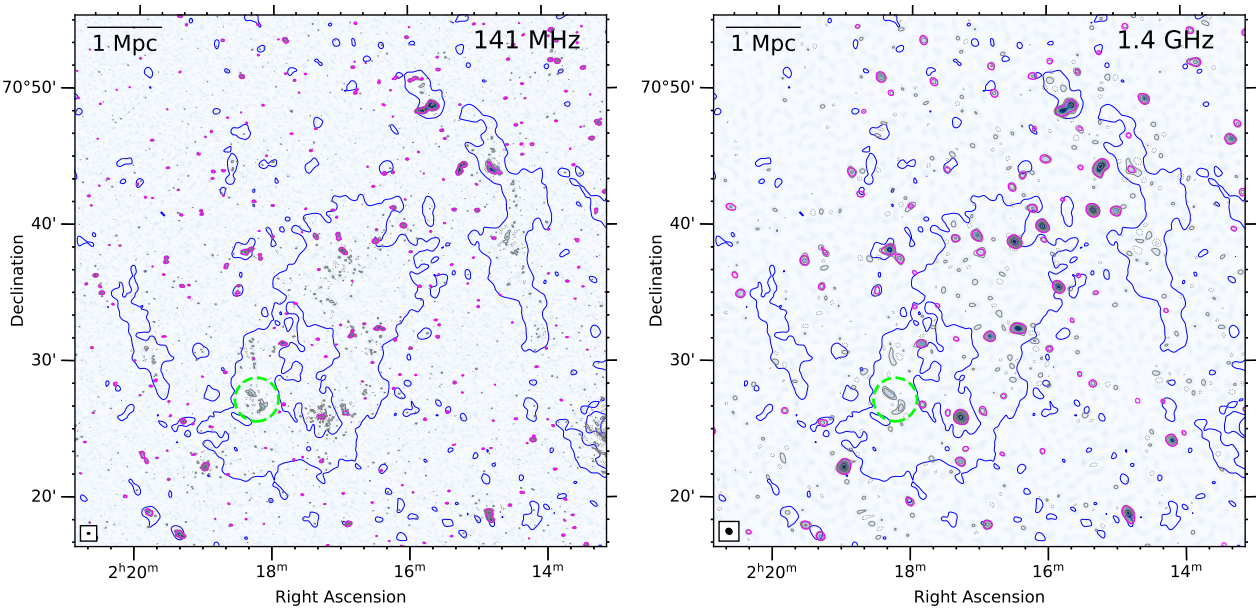

Fig. A.1. LOFAR 141 MHz (*left*) and VLA 1.4 GHz (*right*) high-resolution flat-noise images (i.e. primary beam uncorrected). The contaminating discrete sources, marked with the magenta contours, are removed from the *uv* data. The source in the dashed circle is not included in the subtracted model. The contours are $[1, 2, 4, 8, 16] \times 3\sigma$, where $\sigma_{\rm LOFAR} = 140\,\mu{\rm Jy\,beam^{-1}}$ and $\sigma_{\rm VLA} = 80\,\mu{\rm Jy\,beam^{-1}}$. The blue compact-source-subtracted contour is drawn at 2σ, where $\sigma = 335\,\mu{\rm Jy\,beam^{-1}}$ and the beam size is $45.7'' \times 44.7''$.

Appendix B: Fitting the radio halo with a circular two-dimensional model

The corner plots for the fitting parameters with circular exponential two-dimensional model in Sect. 3.1.1 are shown in Fig. B.1. The maximum likelihood parameters and the uncertainties are estimated using the `emcee` code (Foreman-Mackey et al. 2013).

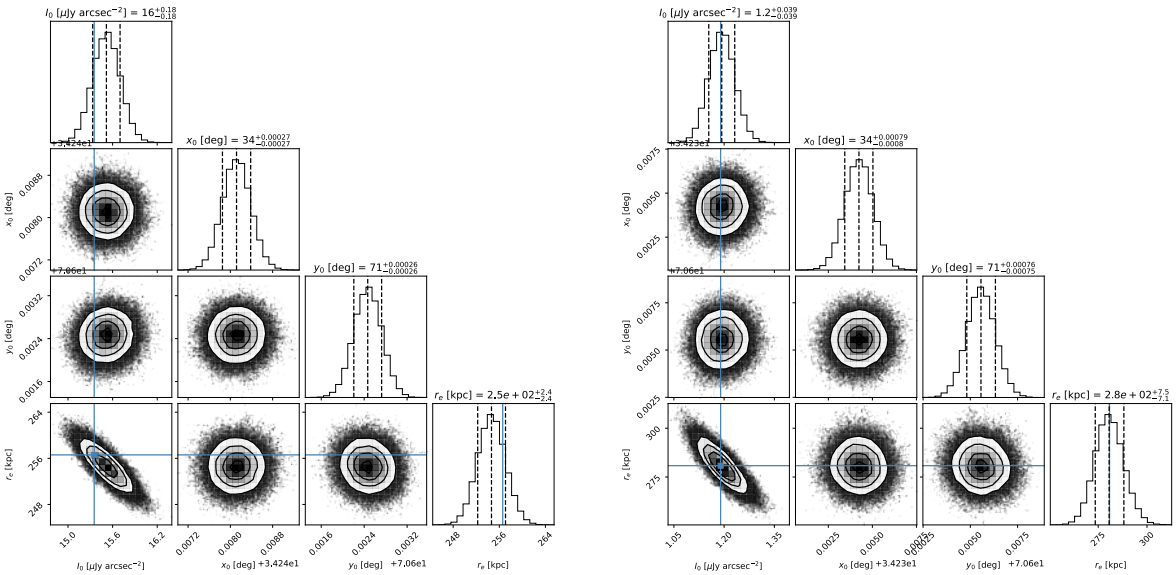

Fig. B.1. Corner plots obtained from the fitting of a two-dimensional circular model to the SB of the radio halo at 141 MHz (*left*) and 1.4 GHz (*right*). The blue lines show the initial estimates for the peak brightness, I_0, and the *e*-folding radius, r_e, by the pre-MCMC fitting. The x_0 and y_0 are the best-fit values in R.A. and Dec. of the halo peak.

Appendix C: Spectral index error maps

In Fig. C.1 we present the spectral index error maps at the resolution of 16″ and 46″. The corresponding spectral index maps of ClG0217 are made using the LOFAR and VLA images that are described in Sect. 2.4.

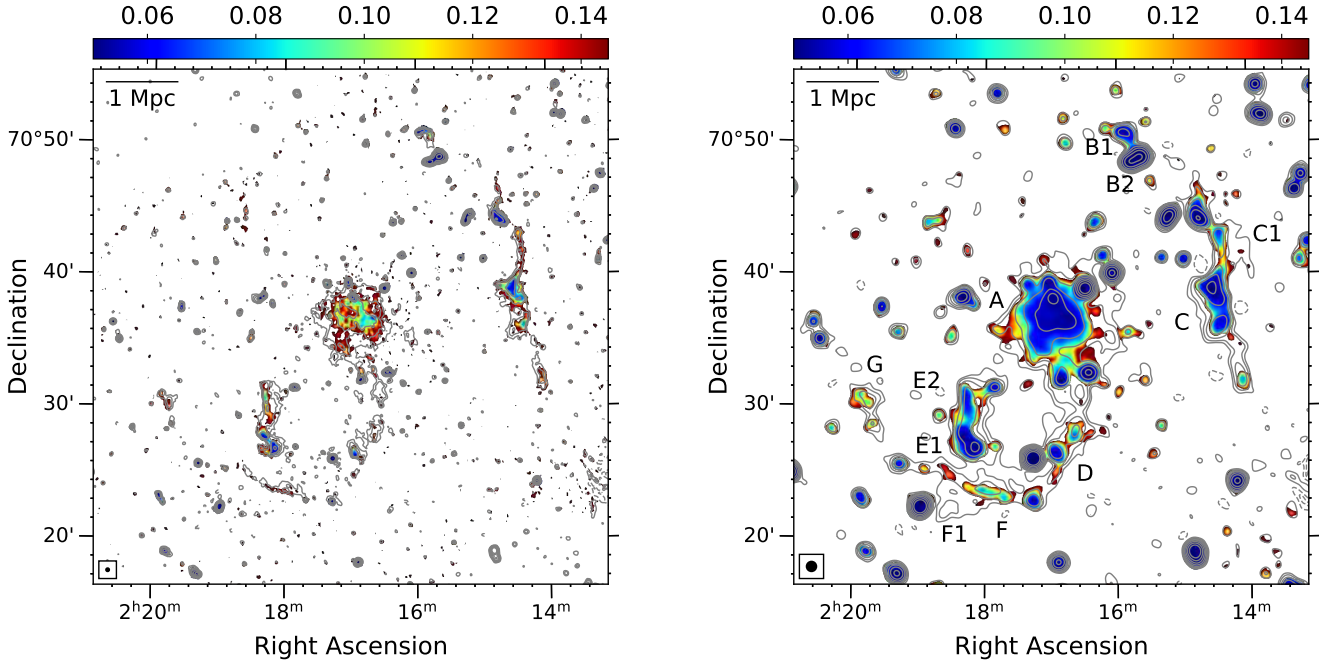

Fig. C.1. Spectral index error maps at 16″ (*left*) and 46″ (*right*) resolutions. The LOFAR 141 MHz contours of $[1, 2, 4, 8, 16] \times 3\sigma$, where $\sigma_{\rm LOFAR}$ = 345 μJy beam^{-1} (*left*) and 190 μJy beam^{-1} (*right*), are overlaid.

Appendix D: Cutout images

To search for optical counterparts of the cluster radio sources, we make cutout Pan-STARRS colour (band y, i, g) images in the regions of sources B1+B2, C, and E in Fig. D.1.

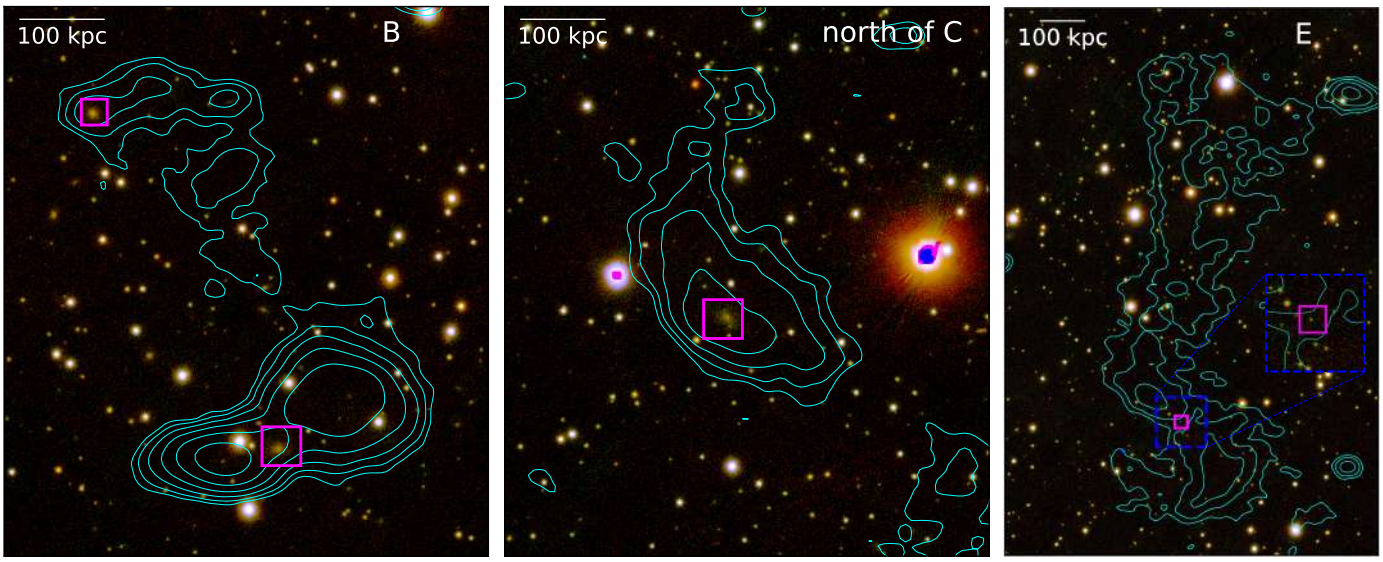

Fig. D.1. Pan-STARRS colour (y, i, g) images of sources B1+B2 (*left*), C (*middle*), and E (*right*). The square magenta regions show the optical counterparts of the radio galaxies. The overlaid image in the *right* panel shows the central region of the southern part of E (i.e. E1).